SPATIAL AND TEMPORAL VARIATIONS OF EARTHQUAKE FREQUENCY-MAGNITUDE DISTRIBUTION AT THE SUBDUCTION ZONE NEAR THE NICOYA PENINSULA, COSTA RICA

A Thesis
Presented to
The Academic Faculty

by

Yan Luo

In Partial Fulfillment
of the Requirements for the Degree
Master of Science in the
School of Earth and Atmosphere Sciences

Georgia Institute of Technology
December 2011

SPATIAL AND TEMPORAL VARIATIONS OF EARTHQUAKE FREQUENCY-MAGNITUDE DISTRIBUTION AT THE SUBDUCTION ZONE NEAR THE NICOYA PENINSULA, COSTA RICA

Approved by:

Dr., Andrew Newman Advisor
School of Earth and Atmospheric Sciences
Georgia Institute of Technology

Dr. Zhigang Peng
School of Earth and Atmospheric Sciences
Georgia Institute of Technology

Dr. Josef Dufek
School of Earth and Atmospheric Sciences
Georgia Institute of Technology

Date Approved: November 11, 2011

ACKNOWLEDGEMENTS

I would like to thank my advisor Dr. Andrew Newman for his great guidance on this thesis and instructing me on how to think critically and insightfully. He leads me to the right path of becoming an independent scientist in the future. I am grateful to Dr. Zhigang Peng and Dr. Josef Dufek, my thesis committee members, for their thoughtful suggestions. I am also thankful to Dr. Marino Protti, Dr. Susan Schwartz and Dr. Lujia Feng for providing useful seismic and geodetic data. I also thank Chenxiao Du, Chunquan Wu, Chastity Aiken, Xiaofeng Meng, Peng Zhao, Kevin Chao, Jamie Convers and Brendan Sullivan for giving me their valuable suggestions on my thesis. Additionally, I thank other faculty and graduate students in our geophysics group at Georgia Tech.

Finally, I would like to greatly thank my parents in China for their love and support.

TABLE OF CONTENTS

LIST OF FIGURES

SUMMARY

The Nicoya Peninsula of Costa Rica is unusually close to the Middle America Trench (MAT), such that interface locking along the megathrust is observable under land. Here, rapid convergence between the downgoing Cocos and the over-riding Caribbean plates at ~85mm/yr allows for observable high strain rates, frequent large earthquakes and ongoing micro-seismicity. By taking advantage of this ideal location, a network of 20 on-land broadband seismometers was established in cooperation between UC Santa Cruz, Georgia Tech, and OVSICORI, with most stations operating since 2008.

To evaluate what seismicity tells us about the ongoing state of coupling along the interface, we must consistently evaluate the location and magnitude of ongoing micro-seismicity. Because of large levels of anthropogenic, biologic, and coastal noise, automatic detection of earthquakes remains problematic in this region. Thus, we resorted to detailed manual investigation of earthquake phases. So far, we have detected nearly 7,000 earthquakes below or near Nicoya between February and August 2009. From these events we evaluate the fine-scale frequency-magnitude distribution (FMD) along the subduction megathrust. The results from this '*b*-value mapping' are compared with an earlier study of the seismicity 9 years prior. In addition, we evaluate them relative to the latest geodetically derived locking. Preliminary comparisons of spatial and temporal variations of the *b*-values will be reported here.

Because ongoing manual detection of earthquakes is extremely laborious and some events might be easily neglected, we are implementing a match-filter detection algorithm to search for new events from the continuous seismic data. This new approach has been previously successful in identifying aftershocks of the 2004 Parkfield earthquake. To do so, we use the waveforms of 858 analyst-detected events as templates to search for similarly repeating events during the same periods that have been manually detected. Preliminary results on the effectiveness of this technique are reported.

The overall goal of this research is to evaluate the evolution of stress along the megathrust that may indicate the location and magnitude of potentially large future earthquakes. To do so, I make the comparison between the FMD and the interface locking. Only positive correlations are observed in the Nicoya region. The result is different from the one derived from the seismic data set that was recorded 9 years before our data. Therefore, to substantiate the causes for the different relationships between the *b*-value and the coupling degree, we need additional data with more reliable magnitudes.

CHAPTER 1

INTRODUCTION

1.1 Overview and Motivation

Earthquake activity usually occurs along plate boundaries with subduction zones creating the majority of great earthquakes (*Mw*>8.0). This is because subduction zones have a large area of lithospheric plates sliding against each other with a negative buoyancy force driving this plate-consuming process ceaselessly. Great shaking of the ground produced by these megathrust earthquakes has been inducing dramatic and catastrophic hazards to coastal population. Hence, it is very important to investigate the evolution of subduction interface locking, which is the process that the fault strain is accumulated on the subduction interface due to elastic loading.

The Costa Rica region is an excellent geological location to investigate those phenomena, because the Nicoya Peninsula of Costa Rica is proximal to the Middle America Trench (MAT). As well abundant existing geodetic and seismic data also provides excellent foundation for this research. I use the 2009 earthquake catalog (from February to August) of this region to evaluate the spatial and temporal variation of frequency of seismicity magnitude distribution. Then I use the seismicity rate distribution as a proxy to study the stress accumulated along the fault. In addition, I also compare the fault interface locking derived by the inversion of GPS modeling with my result of frequency- magnitude distribution (FMD). Finally, I assess the validity of FMD to infer strain accumulation. The results from my FMD are compared with a study of the seismicity 9 years prior. Hence, the spatial and temporal variations of FMD give us a general view of evolution of stress accumulation near the subduction region of Nicoya. It

is significant that the FMD may be useful to indicate the location and magnitude of potentially large future earthquakes.

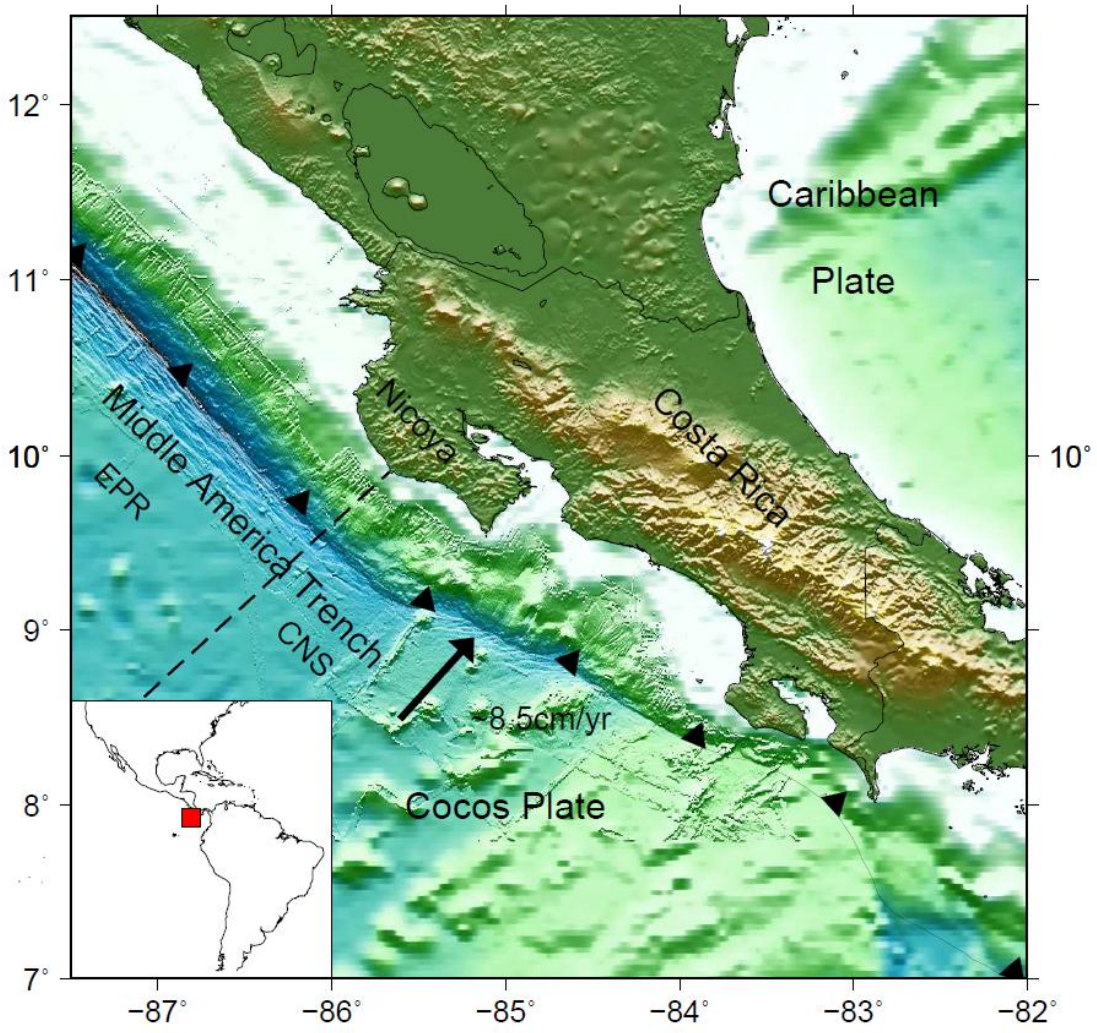

Figure 1: Map of the study region. The Cocos Plate subducting towards the Caribbean Plate along the Middle American Trench near Costa Rica. The arrow shows the convergence direction of the Cocos Plate relative to the Caribbean Plate. The red box on the lower left corner denotes the study area in a larger perspective.

1.2 Tectonic setting

The Nicoya Peninsula offshore is close to the MAT with an approximate distance of 60 km (Figure 1). The Cocos Plate, located on the southwestern side of the MAT, subducts beneath the Caribbean Plate at the rate of 8~9 cm/yr [*Dixon*, 1993; *DeMets*, 2001]. The Cocos Plate contains tectonic and morphological boundaries. Specifically, two subducting oceanic crust plates, the Cocos-Nazca Spreading center (CNS) plate beneath the southern Nicoya and the East Pacific Rise (EPR) plate beneath the northern Nicoya (Figure 1), are characterized with different geologic ages, topography (only on the subsurface in the Nicoya region), movement orientation, and heat flow distribution. The boundary is almost perpendicular to the MAT and cut through the central Nicoya Peninsula [*Barkhausen et al.*, 2001]. CNS, which is characterized by subducted seamounts [*Barkhausen et al.*, 2001, *Husen et al.,* 2003] and relatively rough bathymetry is 15-16 Ma, and the heat flow is about 110-120 mW/m^2. On the other hand, EPR, which is dominated by smoother bathymetry [*Von Huene et al*., 1995; *Protti et al*., 1995a], has the age of 22-24 Ma [*Barkhausen et al.,* 2001], and the heat flow of EPR crust is only 10-40 mW/m^2 [*Vacquier et al*., 1967; *Langseth and Silver*, 1996; *Fisher et al.,* 2001], which is lower than that of CNS. *Newman et al* [2002] identified that the thermal distribution difference corresponds to changes in the up-dip limit of seismogenic zone; activity on the cooler EPR crust is 5 km deeper than that of the warmer CNS crust. In addition, *Spinelli et al*., [2006] suggested that temperature variation at the boundary of these two oceanic crust results in the change of fluid pressure. Specifically, cooler EPR crust along the decollement is characterized by relatively higher fluid pressure. Due to the different origin of these two oceanic crusts, two other interesting features are that the EPR plate

subducts towards Nicoya parallel to the MAT, and that CNS crust subducts almost perpendicularly to the trench [*Barkhausen et al*., 2001]. Previous studies of seismic reflection and refraction data on the Nicoya region suggest a shallow angle of 6 °of the slab interface near the trench; and the angle increases to 35 °by 40 km depth [*Christeson et al*., 1999; *Sallares et al*., 1999, 2001] before reaching to 80 °down-dip of the seismogenic zone [*Protti et al.*, 1995*b*].

1.3 Previous work

Subduction zones are considered to be one of the best locations in studying tectonic phenomena, earthquakes, and other relevant earth sciences. Megathrust earthquakes that occurred near the subduction regions attract the attention of earth scientists and even the general population by the tremendous ground shaking and potentially subsequent tsunami. It is widely accepted that stick-slip mode is the main principle for generating megathrust earthquakes. When the faults slide against each other, static friction will prevent sliding along the interface if static friction is strong enough. After the accumulated stress by plate convergence becomes large enough to overcome the static friction, the rupture along the fault will occur and burst into megathrust earthquakes.

However, the asperity distribution on faults, pore fluid induced by sediment deposition, variable temperature and pressure distribution, and complex topography could influence the occurrence of stick-slip earthquakes. Specifically, the complex characteristics of the combination of CNS and EPR near the Nicoya area proves that the locking of seismogenic zones cannot be simply interpreted. In detail, *Newman et al*.

[2002] discovered that the up-dip limit of seismogenic zone near Nicoya is shifted along the strike direction at the boundary of EPR and CNS. This phenomenon can be interpreted that the difference of plate characteristics allows the heterogeneity of fault locking.

The geodetic modeling based on GPS data is a useful and convenient technique for studying the coupling variance of seismogenic zones. *Lundgren et al*. [1999] organized three GPS campaigns on 23 sites that were distributed in Costa Rica in 1994, 1996 and 1997. Most sites were occupied for 3 to 5 days, while some of them were occupied up to 2 weeks. By testing the locked segment of the downgoing plate by applying the dislocation model of *Okada* [1985], the authors estimated that the fault is locked 70 to 95 km away from the trench. In addition, they established an inversion model to produce the fault slip rate by assuming that the downgoing interface is composed of seven continuous planes with variable depths and dip angles. Eventually, they extrapolated that the central and southeast portion of Nicoya is highly locked. *Norabuena et al.* [2004] continued to collect GPS campaign data in this area in 2000 (3 to 5 days of observations at most sites from January to February 2000). Moreover, they set up new monuments and occupied in order to obtain abundant GPS data of ground movement for future research. They improved the inversion model by considering both the elastic deformation and permanent deformation. Underneath the central Nicoya, *Norabuena et al.* [2004] estimated a ~60% locked patch at 14+/-2 km depth and a 35% locked patch at 39+/-6 km depth. Before applying the improved model, *Norabuena et al.* [2004] defined the geometry of plate interface as three adjoining plane segments with different dips. In addition, they also estimated the northwest motion of fore-arc block with a rate of 8+/-3mm/yr.

Furthermore, *Feng et al.* [2010] utilized old GPS campaign data of Nicoya in 1996, 2000, and 2003, and the new GPS campaign data in 2010 to obtain a new inversion of fault slip. They estimated that a fully locked (back slip ~8cm/yr) interface is distributed mainly at the central Nicoya coastline, and the northwest and southeast offshore regions of Nicoya. Compared with the results from *Norabuena et al*. [2004], the maximum coupling degree has increased from approximately 60% to 100%. There are a few reasons to cause the difference of coupling distribution. Longer time span of GPS displacement data utilized by *Feng et al*. [2010] yields a better resolution to the seismogenic interface coupling. Also, the different megathrust interface models adopted by different groups could result in the variations of interface locking. The locking pattern derived from *Feng et al* [2010] is similar to the one derived by *LaFemina et al.* [2009], who combined the episodic and continuous GPS data from 1993 to 2005. Overall, these results prove that the subducting interface under the central Nicoya coastline is highly coupling.

However, the GPS technique has a disadvantage on determining the locked patches on the fault. Generally speaking, the geodetic modeling is dependent on the accuracy of slab geometry and the assumption of homogenous material. Some previous studies applied micro-seismicity to infer the stress distribution along the megathrust. For instance, *Wiemer and Benoit* [1996] applied the mapping of frequency- magnitude distribution (FMD) of micro-seismicity in depth under the Alaska and New Zealand subduction zones. They interpreted that the region with high *b*-values on the FMD map is associated with the high pore pressure. It is mainly because of the magmagenesis influences, which can reduce effective stress. On the other hand, *Sobesiak et al.*, [2007]

and *Ghosh et al.,* [2008] made the FMD mappings only using earthquakes along the interface near subduction zones. Specifically, *Ghosh et al*. [2008] interpreted the region with low *b*-values on the FMD map near the Nicoya subduction megathrust is associated with the increased interface locking, which was modeled by *Norabuena et al* [2004]. Furthermore, *Ghosh et al*. [2008] suggested that the FMD could be used as an effective proxy for studying the stress regime along the fault. I will continue to employ this technique to evaluate the location and magnitude of micro-seismicity that occurred in the same area as investigated by *Ghosh et al.* [2008]. However, the earthquake catalog that I am using is 9 years later than theirs, and an earthquake detection technique is applied to gain a more complete catalog.

CHAPTER 2

DATA AND METHODOLOGY

In this thesis, the completeness of the earthquake catalog is a prerequisite for investigating the megathrust stress regime, which will be discussed later. However, it is common that numerous earthquakes, especially the ones with relatively small magnitude, are missing in existing earthquake catalogs. There are a few factors that may cause this incompleteness, such as negligence when manually picking events, small magnitude events being masked by the coda wave of large earthquakes with higher amplitudes. Here, a matched filter detection algorithm is applied to evaluate repeating events. The main idea of this method is to calculate the cross-correlation (CC) coefficient between the prepared template and continuously recorded waveforms. When the waveform CC value is above a defined threshold value, we will record the detection of a missing event at the corresponding time. The matched filter technique has been successful in identifying non-volcanic tremor and low-frequency earthquake beneath Shikoku, Japan [*Shelly et al*., 2007], as well as for detecting aftershocks of the 2004 Parkfield earthquake in California [*Peng and Zhao,* 2009]. *Du et al.* [*in prep*.] also applied this algorithm for detecting aftershocks of the 2000 Nicoya outer-rise earthquake across the Middle America Trench. In this thesis, the analysis procedure of detecting missing events generally follows the steps of *Du et.al.* [*in prep.*].

2.1 Seismic data and processing

In order to systematically study the megathrust stress regime of Costa Rica using micro-seismicity, a network of 20 on-land broad-band seismometers was established in

cooperation between University of California, Santa Cruz, Georgia Institute of Technology, and Observatorio Vulcanológico y Sismológico de Costa Rica (OVSICORI), with most stations operating since 2008. In this study, only 14 stations are in good working conditions (Figure 2). Fortunately, the Nicoya Peninsula is close to the MAT and the initial angle of the downgoing plate is shallow, therefore the 14 working

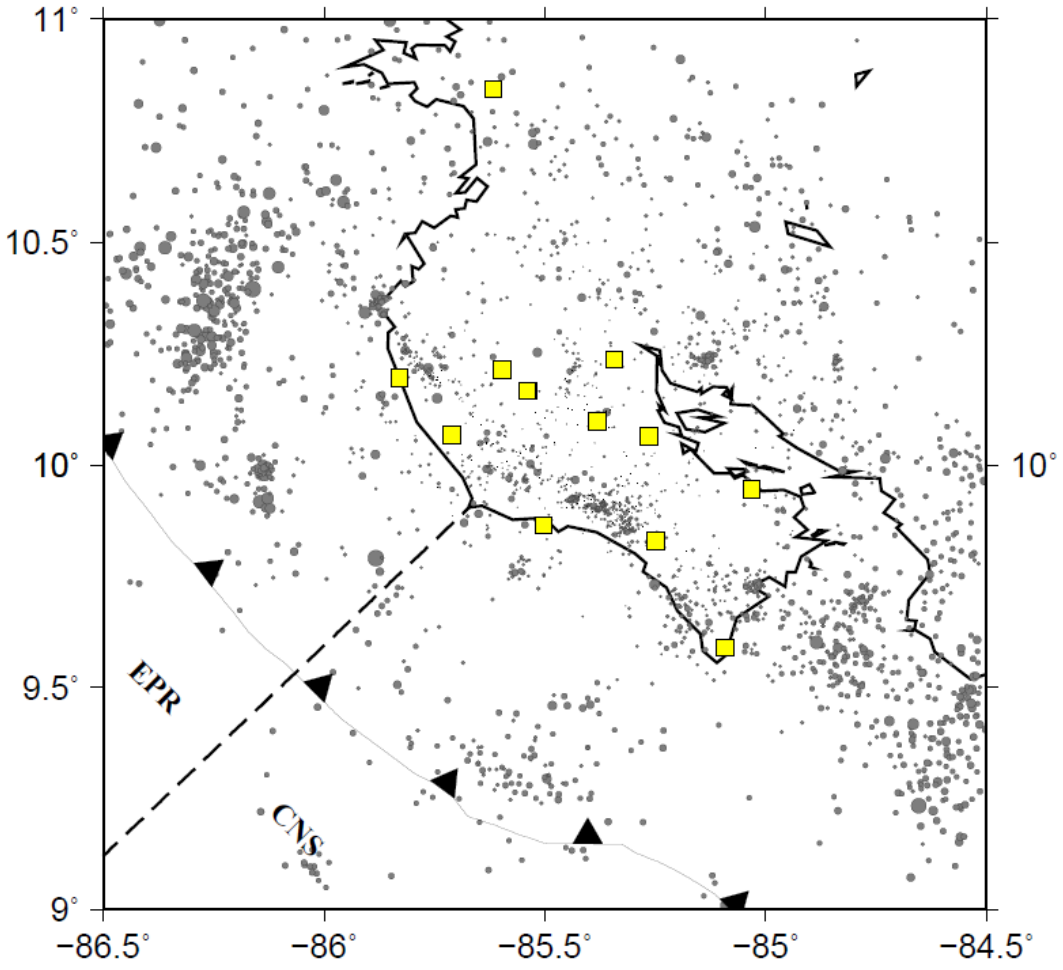

Figure 2: 14 on-land broadband seismometers, which are denoted by yellow squares, are distributed on the Nicoya Peninsula. Since 2 stations overlap with other 2 stations, only 12 stations are shown in this graph. Grey circles are the earthquakes recorded from February to August 2009. Dash line is the transitional boundary between EPR and CNS. Saw-soothed curve is the Middle America Trench.

seismometers installed on the Peninsula can capture very small earthquakes, and the geometry of the seismometer distribution can also well constrain the location and magnitude of earthquakes beneath Nicoya [*Newman et al*., 2002; *DeShon and Schwartz*, 2004; *Norabuena et al*., 2004; *DeShon et al*., 2006].

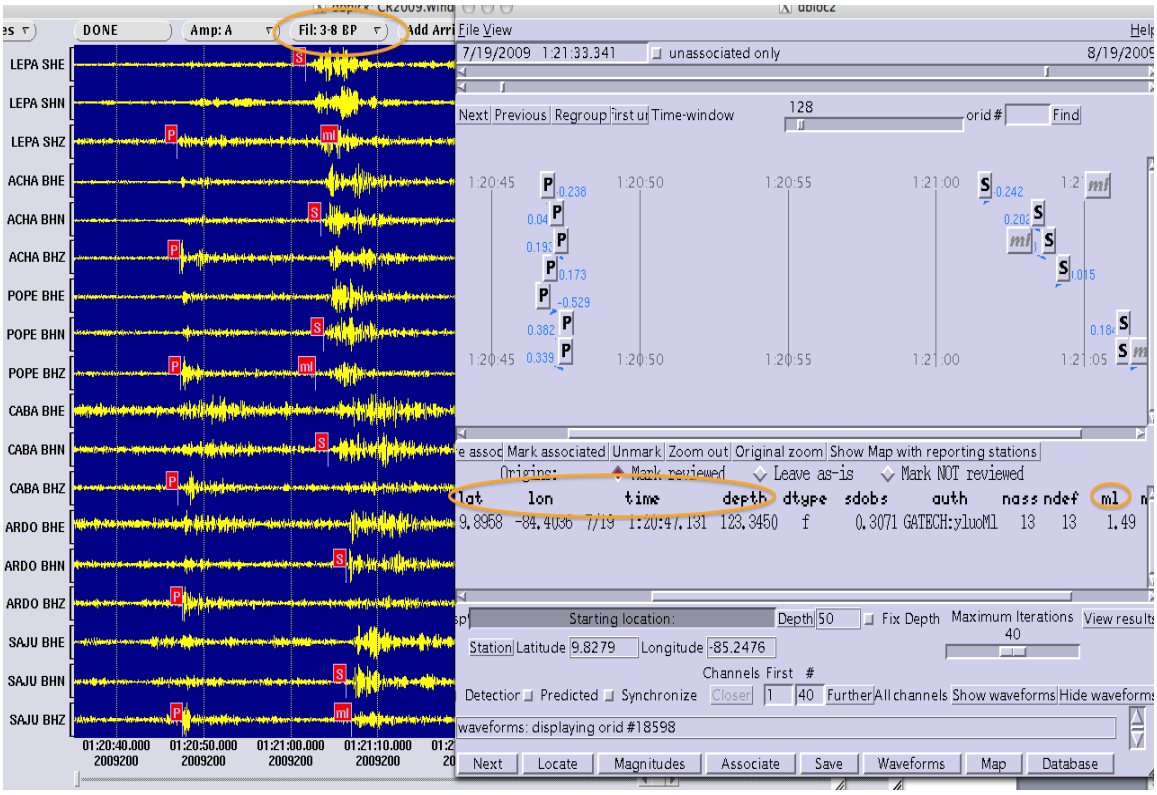

Figure 3: Program interface image of Antelope 4.11. 3-8Hz broadband filter is applied on the seismograms. By manually picking the P- and S-arrival phases, the occurrence time, location and local magnitude of earthquake can be determined by the integrated algorithms within Antelope.

Because of the high level of cultural and coastal noise, the automatic detection of earthquakes was only partially successful in the region. Thus, we manually identified the *P*- and *S*-wave arrival times in Antelope Relational Database System, which was developed by Boulder Real Time Technologies, Inc. (http://www.brtt.com). Since the one

dimensional velocity model is integrated in the Antelope system (Figure 3), we have detected almost 7,000 local and regional earthquakes below or near Nicoya by applying this velocity model. Afterward, we relocated the hypocenter of the detected events using the 3-D velocity model of V_p and V_p/V_s, which was derived by *DeShon et al* [2006]. This process was executed by running a FORTRAN program, *SIMULPS*12 [*Thurber,* 1983]. Because of the inadequate phase picking and the spatial limitation of *DeShon*'s velocity model [*Ghosh et al.,* 2008], ~300 local events were removed from the catalog after running *SIMULPS*12. In order to guarantee the accuracy of the event location, we kept 80% of the original earthquakes (~5,400) with better location accuracy for the analysis. Thus, we removed the earthquakes (~1,300) with horizontal error higher than 6.7 km and vertical error larger than 5km.

In order to verify the reliability of the calculated local magnitudes determined by the algorithm of Antelope, we compared the magnitudes determined by Antelope with those of the ANSS (Advanced National Seismic System) catalog. Furthermore, we also requested the catalog from Observatorio Vulcanológico y Sismológico de Costa Rica (OVSICORI) to make additional comparison of magnitudes. Because the catalog from ANSS is worldwide, we only requested the catalog of earthquakes with magnitude larger than 3, which is a relatively large magnitude compared to our catalog. The comparison (Figure 4, a) among 12 sparse events shows that the slope of the fitting line is about 0.477+/-0.2959. The result does not show a good fitting line with a slope of 1 because the magnitudes from ANSS are mostly moment magnitudes, which are usually higher than local magnitude. Furthermore, the comparison of magnitudes from our catalog and OVSICORI (Figure 4, b) shows that the fitting slope is about 0.69+/-0.09. However,

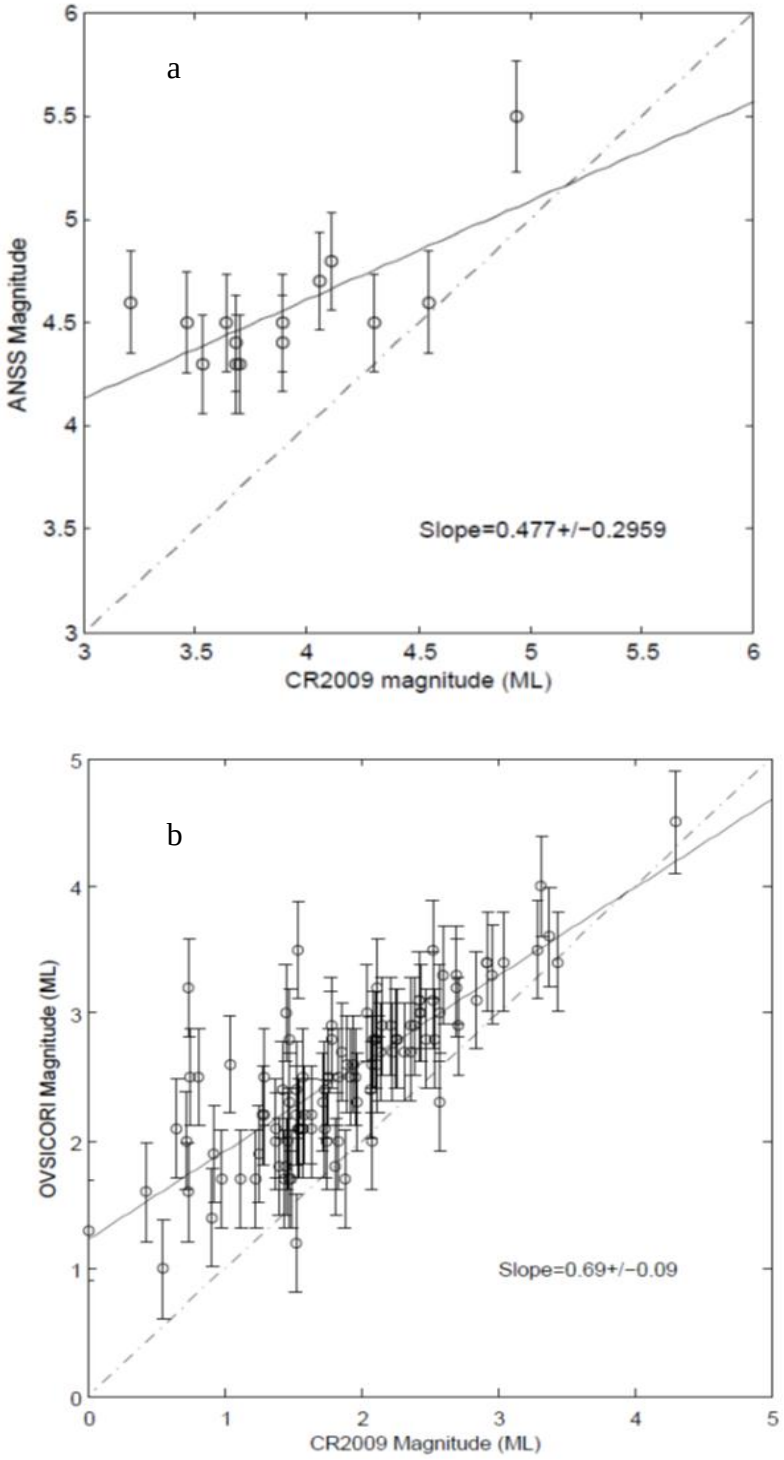

Figure 4: (a) Comparison between the local magnitude determined by Antelope and the magnitude downloaded from ANSS (most of them are moment magnitude). A solid line is the best-fit line with slope of 0.477; (b) Comparison between our local magnitude and local magnitude of OVSICORI. The best-fit line has a slope of 0.69. Dashed lines represent the slope of 1. Error bars are the standard deviations of the error when using least square method to predict the line.

OVSICORI stations are mainly distributed on the Costa Rica mainland. The geometry of seismometer network might have influence on the computation of earthquake location and magnitude. Compared with our seismic network, the different geometry of seismometers may cause the different results on magnitude.

In this study, I focus on the interface beneath the Nicoya Peninsula region, and I intend to verify the FMD pattern on the interface between the Cocos plate and the Caribbean Plate. The interface below the depth of 70 km goes beyond the peninsula and reaches to the mainland of Costa Rica, rather than just underneath Nicoya [*Norabuena et al*., 2004]. Overall, I keep the qualified ~3,000 events in the catalog for further investigation.

2.2 Processing of the earthquake waveform template

By following the procedure of detecting new events introduced by *Du et al.* [*in prep*], I calculated the signal to noise ratio (SNR) for each one of the components from those qualified events. The waveforms of selected events with a SNR larger than 12 and with more than 12 components (4 stations) were kept as templates. Each template is 60 seconds in length. The signal amplitude value was chosen as the 4-second time window starting from 2 seconds before the *P* arrival for vertical component and 2 seconds before *S* arrival time for horizontal components. On the other hand, the noise amplitude value was selected from the 4-second time window beginning 6 seconds prior to the *P* arrival time. A 2-8 Hz bandpass filter is applied to the templates and continuous waveforms. Overall, 858 events are selected to be the templates for the following analysis.

After the waveform templates were obtained, I scanned them through the continuous seismic data for each station and component, calculating the CC values. The continuous data was recorded between February and August 2009, which is the same period that the manual investigation went through. For each component of waveform, a 4-second sliding window, which begins from 2 seconds before *S*-wave arrival to 2 seconds after, was extracted for scanning through the corresponding continuous waveforms in an increment of 0.04 seconds, which is the sampling interval of the data. Then, the correlation coefficient was calculated for each point of each component, and CC functions were stacked to generate a mean CC array by shifting the *S* arrival to the origin time. Missing events could be detected by finding high CC value that is above a threshold. In our case, 9 times the median absolute deviation (MAD), which is approximately 0.3, was selected as the threshold. Because the waveforms of the template and detected events are similar between several recording stations, the hypocenter coordinates should be very close or identical. I, therefore, assumed that the detected earthquake has the same location as the template event.

Local magnitude (M_L) of micro-seismicity was used in the catalog in this thesis. The scale of M_L is proportional to the logarithm of the largest S wave amplitude, and to the logarithm of the distance between station and hypocenter [*Stein and Wysession*, 2003]. The ratio between the logarithms of *S* wave amplitude can determine the local magnitude of the new event. It can be described as

$$M'_L = M_L + \log(R)$$

where M'_L is the magnitude of the new events, M_L is the local magnitude of the template earthquake, and R is the median ratio of the largest S wave amplitude between continuous

data and template waveform for all channels. In detail, a 4-second window beginning 2 seconds prior to the *S* arrival time is selected to find the maximum amplitude of *S* wave.

2.3 Results

In total, I have detected 5,232 events that were not listed in the original catalog after I removed the multiple detections. Figure 5 shows an example of a newly detected event on February 7, 2009. There is one peak of mean CC values that is above the threshold of 9*MAD (~0.38). It also plots the waveforms of continuous data and detected events with the average CC value of 0.73. The detected new event with the largest CC in Figure 5 occurred at 09:59:37.

Even though I detected more than 5,000 events that were not included in the original catalog, only 3,138 events have magnitude larger than 0. This can reflect the fact that the micro-earthquakes with relatively weak waveform signal and high SNR still can be identified. By following the similar steps of *Ghosh et al*. [2008] on determining the FMD in the same region, I continue with the screening procedure for generating subset catalog used in this thesis. Due to the geometry of seismometer distribution on the Nicoya, I used the horizontal boundaries that only cover the peninsula region and the nearby coast area. This area is bounded by the following four points (Figure 6):(86.2 °W, 10.125 °N), (85.2 °W, 9.35 °N), (84.6 °W, 10.05 °N) and (85.625 °W, 10.8 °N). Thus, earthquakes within these boundaries get better constrain and accuracy. Since the accumulative stress on the fault might produce the micro-earthquakes, the earthquakes that occurred out of the downgoing slab might be less relevant to be used for the next step. By referencing to the 2D plate boundary model from *Norabuena et al*. [2004], I defined a parabolic function to best fit the boundary model (Figure 7). I used 20 km as

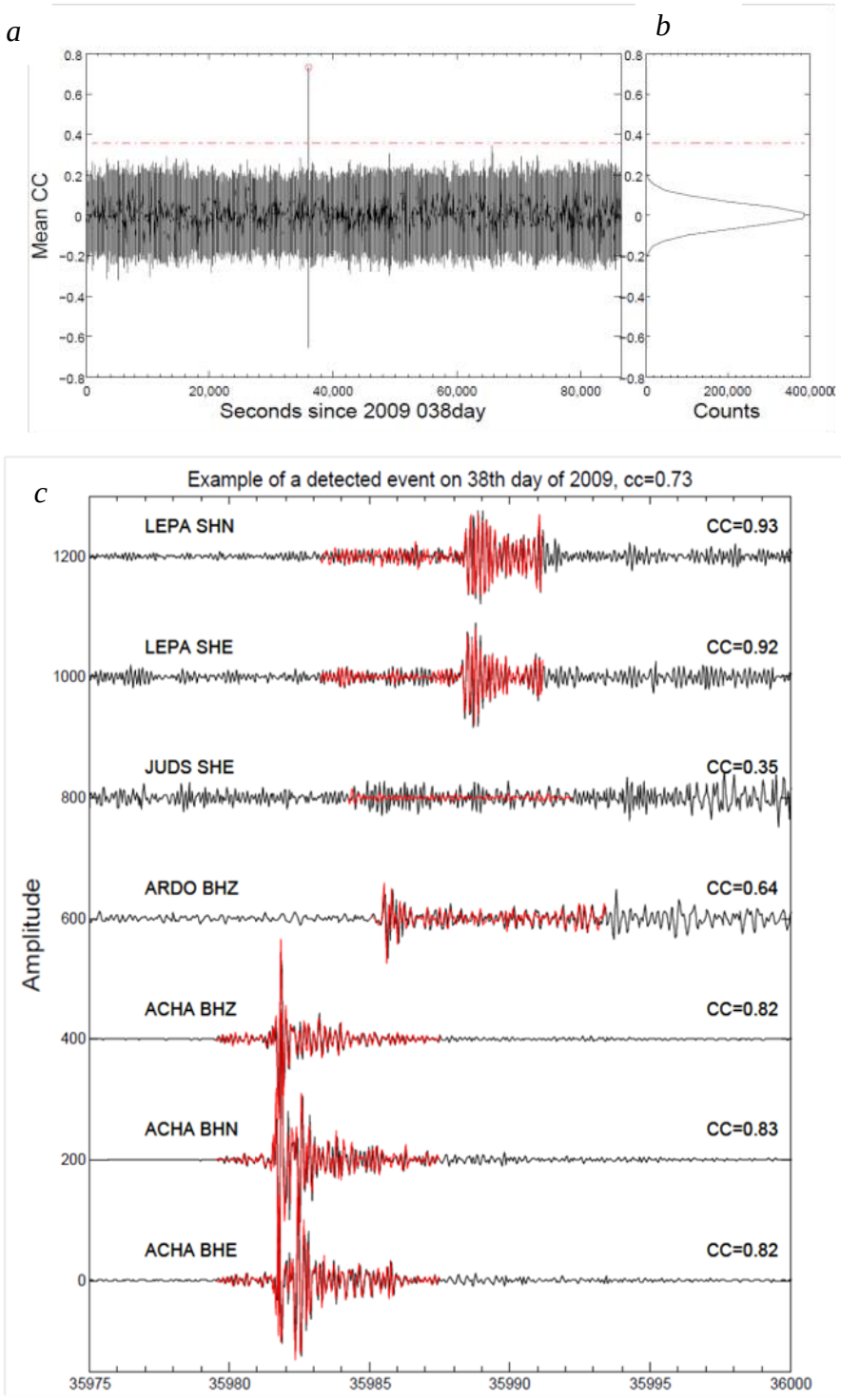

Figure 5: Example of a detected earthquake. a, Mean cross-correlation functions for the template event 2009059063629 (occurred at 06:36:29 on the 59th day of 2009). The red dash line labels the threshold of 9 times MAD, and the red circle corresponds to the detected event at 09:59:37 on February 7, 2009. b, The histogram of the mean correlation

coefficient functions. c, Continuous waveforms are shown in black, and template waveforms are displayed in red. The detected event was recorded by 7 components from 4 stations. Corresponding CC values are shown on the right sides, respectively. Because the waveforms amplitude of template and detected events are different, the template waveform has been shrunk to 0.57 times of its original form.

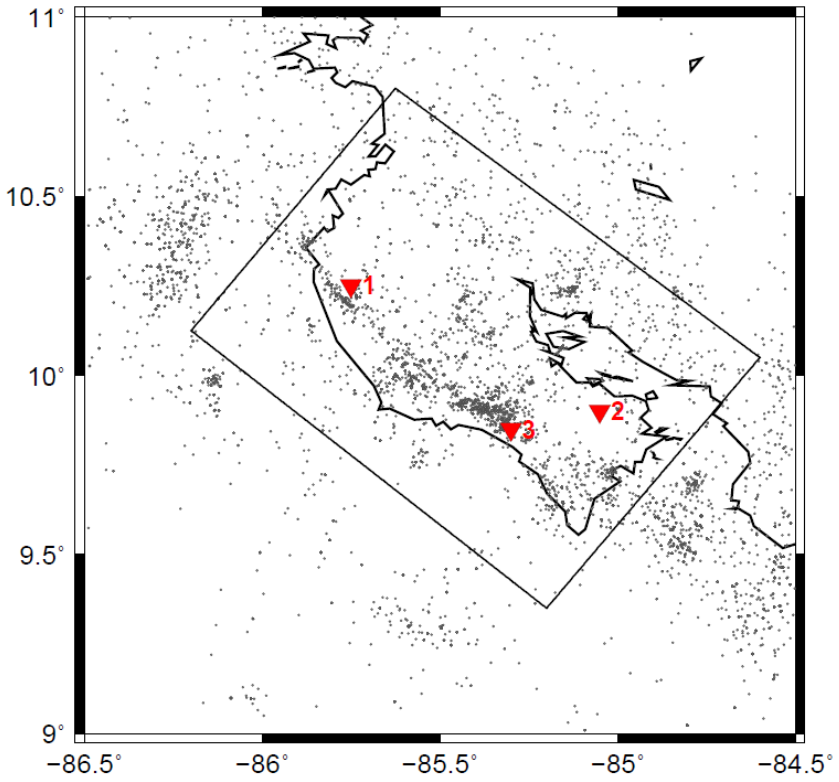

Figure 6: The solid box denotes the focus region, in which earthquakes will be used for further screening process. Three red triangles, 1, 2 and 3, respectively denote regions surrounded by modest, high and low density of seismicity.

the slab thickness [*Ghosh, et al.*, 2008]. Then a thickness of 10 km above and below the parabolic function was respectively applied to generate an approximation of an interface slab.

There is a coordinate transformation from the geodetic coordinate to the local Cartesian coordinate when creating the parabolic boundaries. I defined (85.5 ºW, 9 ºN) as the origin of this coordinate system, and set a Y-axis that is approximately parallel to the

trench, and set an X-axis perpendicular to the Y-axis and pointing to the northeast direction (azimuth angle is 45 degrees). Here, Z-axis is orthogonal to the XY plane and pointing to the earth interior. And the two boundary curves are

$$y = -0.01(x - 30)^2 - 10$$

$$y = -0.01(x - 40)^2 + 15$$

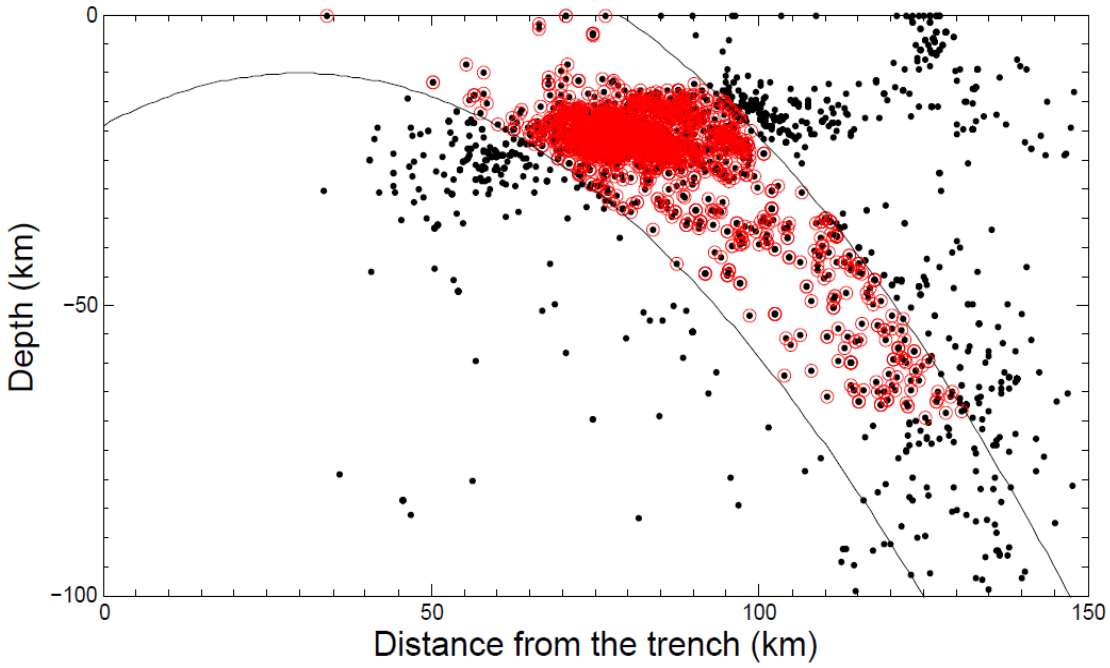

Figure 7: The cross-section view of seismicity underneath Nicoya. Two parabolic curves are the upper and lower boundaries of defined slab. Red circles with a black center point represent earthquakes (depth<70km) that occurred with the parabolic boundaries of subducting slab. Black dots out of the slab are earthquakes that are in the box of Figure 6 but not be used for further study. X-axis is perpendicular to the trench and parallel to the sea level. Y-axis is the depth that is lower than the sea level.

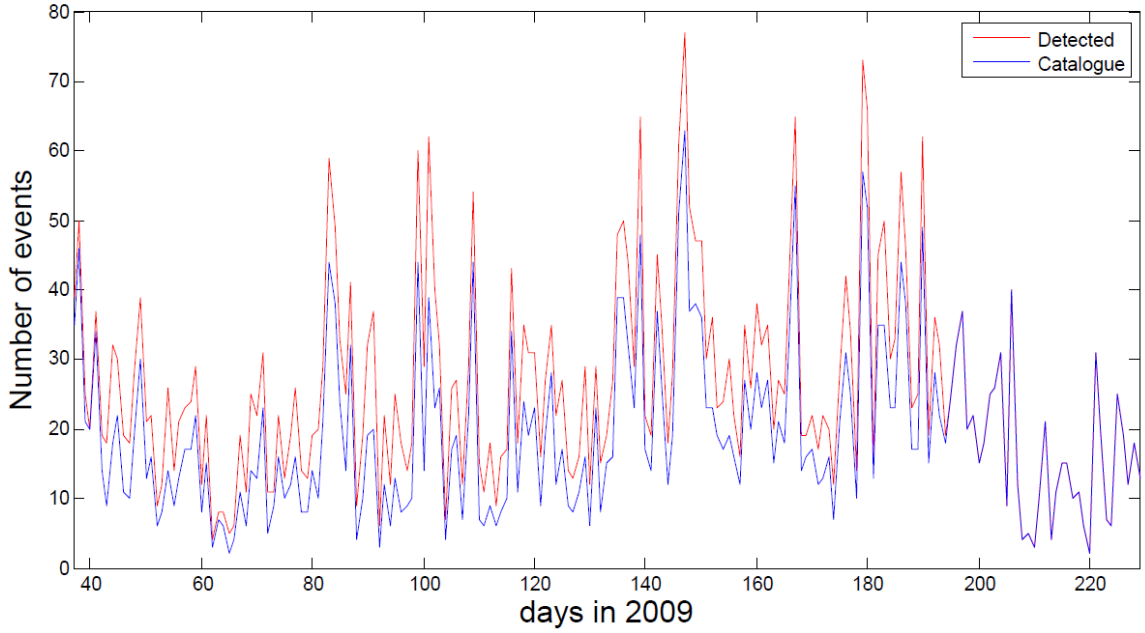

Figure 8: A comparison of number of slab-bounded earthquakes per day from the detected (red) and original (blue) catalogs.

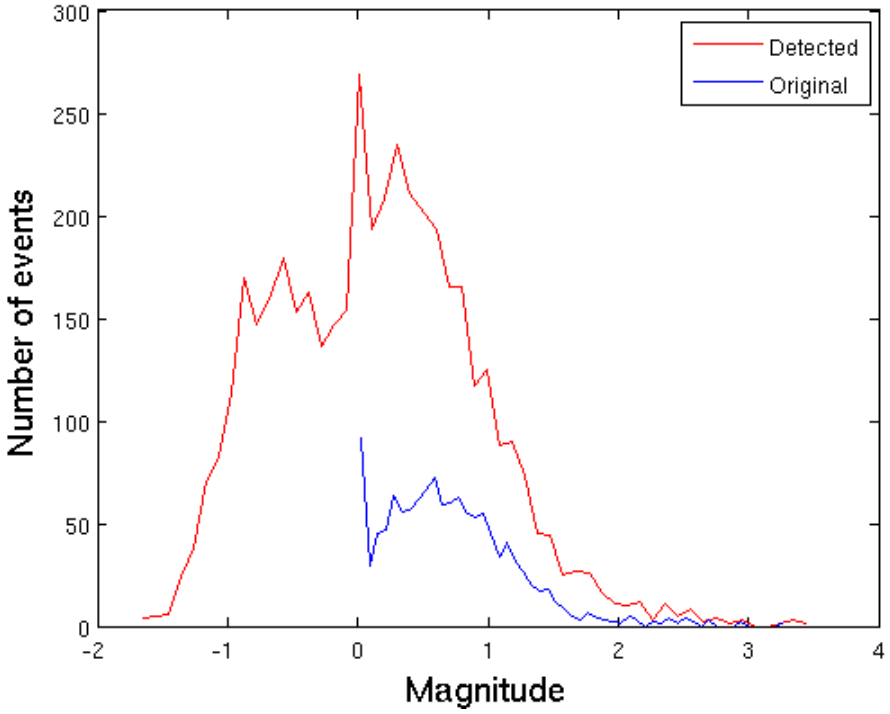

Figure 9: Histogram of earthquake magnitude of events that occurred in the defined slab before (blue curve) and after (red curve) applying the matched filter technique.

After employing the boundary screening procedure, only 1,467 events listed in the original catalog were still kept. However, there were still 2,880 newly detected events that satisfied the standards of boundaries and errors. Figure 8 plots the comparison of earthquake numbers per day in the original catalog and in the newly generated catalog that only contain the earthquakes within the slab. Due to the code problems that recording times were saved in an inappropriate format, the origin times of detected events are getting more and more offset. For the last one or two months, the offset can reach up to 10 seconds. Thus, the computation of magnitude might underestimate the real magnitude. In addition, I also plot the histogram (magnitude interval is 0.1) comparison between the magnitudes in the original and the newly generated catalog in Figure 9. It shows that the detection algorithm detected more than 2,000 events with magnitude less than 0. Still, the auto-detection algorithm observed more (>50) events when the magnitudes are between -1.2 and 1.1. Not too many events with magnitude larger than 2 have been detected by the matched filter method. And only 4 earthquakes (magnitude >3) have been observed by the auto-detection. Overall, there are 87% events with magnitude less than 1and 98.5% events with magnitude less than 2 in the new catalog.

Overall, 4,347 earthquakes within the interface are stored in a final catalog for analyzing the frequency-magnitude distribution.

CHAPTER 3

SEISMICITY RATE AND INTERFACE LOCKING

3.1 Introduction

Grasping the knowledge of recurrence time of earthquakes, especially large earthquakes, is considered to be one of the most significant and challenging questions in the science of earthquakes. The Gutenberg-Richter law [*Gutenberg- Richter*, 1944; *Ishimoto and Iida*, 1939] describes the relationship between the number of earthquakes and their magnitude in any given region. The equation can be expressed by $\log N = a - bM$, where N is the cumulative number of events greater than or equal to the magnitude (M); a and b are constants [*Gutenberg-Richter*, 1944; *Ishimoto and Iida*, 1939]. Thus, the slope of this relationship, the *b*-value, can reflect the ratio of small to large earthquakes. Generally, the worldwide average *b*-value is about 1 [e.g., *Stein and Wysession*, 2003].

Some scientists have proposed that the *b*-value reflects the stress regime. For instance, *Scholz* [1968] performed the experiments by using different rock materials and applying different stress in the laboratory, and the results showed that higher stress applied on the rock created lower *b*-values (<1). Furthermore, several other lab experiments also have been conducted for understanding the physical meaning of the *b*-value [e.g. *Warren and Latham*, 1970; *Wyss*, 1973; *Rabinovitch et al*., 2001, etc.]. *Schorlemmer et al*. [2005] also collected global earthquake catalogs from different fault regimes, such as normal, strike-slip and thrust faults. They found that the *b*-values are usually the highest near the normal fault and that thrust faults are usually characterized with lower *b*-values. Moreover, based on these results obtained from the global catalogs,

they also postulated that the *b*-value could be utilized as an indicator of differential stress.

Specifically, *Wiemer and Benoit* [1996] applied the mapping of frequency-magnitude distribution (FMD) in depth near Alaska and New Zealand subduction zones. They interpreted that the high *b*-value areas on the slab profile are associated with the high pore pressure for the reason of magmagenesis, which induces lower effective stress. Whereas *Sobesiak et al.,* [2007] and *Ghosh et al*., [2008] made the FMD mappings near the subduction zones that are not associated with arc volcanism. Specifically, *Ghosh et al.* [2008] interpreted that the low *b*-value region on the Costa Rica subduction megathrust during the interseismic period is associated with the increased interface locking, which was modeled by *Norabuena et al* [2004]. However, *Sobesiak et al.,* [2007] correlated the high *b*-value and the positive gravity isostatic residual (IR) field after the *Mw*=8.0 Antofagasta earthquake near the subduction zone in Northern Chile. Because the subducting oceanic plate intruded the uplifted batholith structure beneath the continental crust after the main shock, they explained the increased IR as an enhancement of local and regional mass distribution. It appears that these authors obtained opposing results on how to interpret the *b*-values. It is possible that the aftershocks with small magnitude in just 2 months after the main event in Northern Chile may increase the *b*-values. After all, earthquakes happened in the interseismic period, which is before the occurrence of large earthquake, are probably more useful to indicate the stress regime for investigating the evolution of interface locking.

3.2 Methodology

After developing the catalog, I input the subset catalog of 4,347 events into a matlab program named '*bval*', which was developed by *Ghosh et al.,* [2008]. This

program can be used to make grids on the region that are interested, to search earthquakes nearby each grid node by setting the number of events that are involved into the *b*-value determination, and to calculate *a*- and *b*- values, completeness magnitude, and relevant errors by using least square regression (LSR) and maximum likelihood estimation (MLE) [*Aki*, 1965; *Utsu*, 1965].

Here, LSR method is a simple mathematical method. It only determines the fitting line by getting the minimum summation values of squared differences between the estimated line and individual points [*Scheaffer and McClave*, 1986]. On the other hand, the MLE determines the *b*-values by equation

$$b = \log e / (\bar{M} - M_c)$$

where $\bar{M}$ is the mean magnitude, and *Mc* is the completeness magnitude, below which the magnitude is excluded from the calculation of the *b*-value. Hence, the determination of *Mc* for MLE is the key to influence the deviation of the *b*-value. *bval* uses maximum curvature method (MCM) [*Wiemer and Katsumata*, 1999; *Wiemer and McNutt*, 1997] to get an initial *Mc*. Here, MCM takes the highest point of the curvature of the non-cumulative FMD as *Mc*. Using the initial *Mc*, *bval* employs the goodness of fit method to determine a new *Mc* [*Wiemer and Wyss*, 2000].

I assign 0.025 °× 0.025 °as the horizontal unit grid to map the FMD. Each grid would search the nearest events in a vertical cylindrical volume. In order to obtain an optimal number of sampling events for each node, I tested the variations of *b*-value and sampling radius for grid nodes 1, 2 and 3 in Figure 10 where the event densities are different. Here, nodes 1, 2 and 3 respectively represent the regions surrounded by modest, high and low density of seismicity. In Figure 10 (top), *b*-value is not so stable after

counting 170 events to perform the computation of *b*-values when the testing node located at modest density of seismicity. The *b*-value drops from 1.0 to 0.6 when the sampling size increases from 170 to 200. The large earthquakes far from the node 1 might decrease the *b*-value when increasing the sampling radius. This might cause the smear phenomenon of *b*-values on the map. However, more data (sampling size of 200) in the subset catalog is still more statistically reliable than the less data (sampling size of 170) without sacrificing too much sampling radius. Besides, the sampling radius does not exceed 28 km for these 3 nodes when sampling size is around 200. In particular, large sampling area may induce inaccurate reflection of local *b*-value for each grid. I assign set 200 as the sampling size to calculate *b*-values for each individual node.

3.3 Results

The overall *b*-value (Figure 11 top) for the subset catalog is 1.03+/-0.047 by using MLE. Meanwhile, the overall *b*-value (Figure 11 bottom) computed by LSR is 1.08+/-0.082. The *Mc* value is 1.01 by applying the MCM and goodness of fit method. The results of the *b*-value determined by MLE for grid nodes 1, 2, and 3 by using the subset catalogs of nearby 200 events are shown in Figure 12. It is worth noting that the overall *b*-values are close to that of the global average [e.g. *Stein and Wysession*, 2003], which is about 1. However, the overall *b*-values in this thesis are still higher than those of the published subduction zone *b*-values, which are between 0.5 and 0.8 [*Bayrak et al*., 2002]. The difference between the global *b*-value and the one calculated from Nicoya megathrust interface may attribute to a couple of reasons. In our case, we employed a local catalog that only spanned approximately six months. We also only used the events

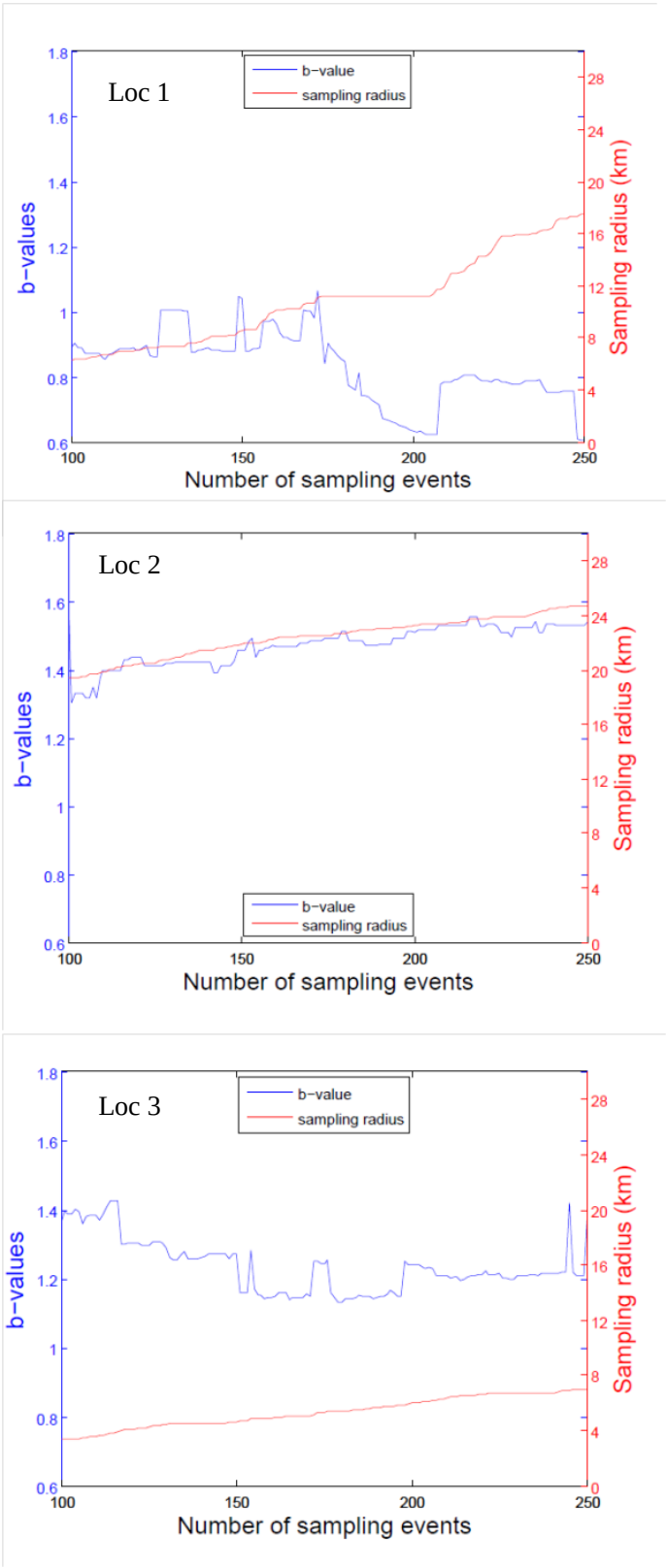

Figure 10: Variation of *b*-values and sampling radius when changing the number of sampling events at location 1, 2, and 3 in Figure 6.

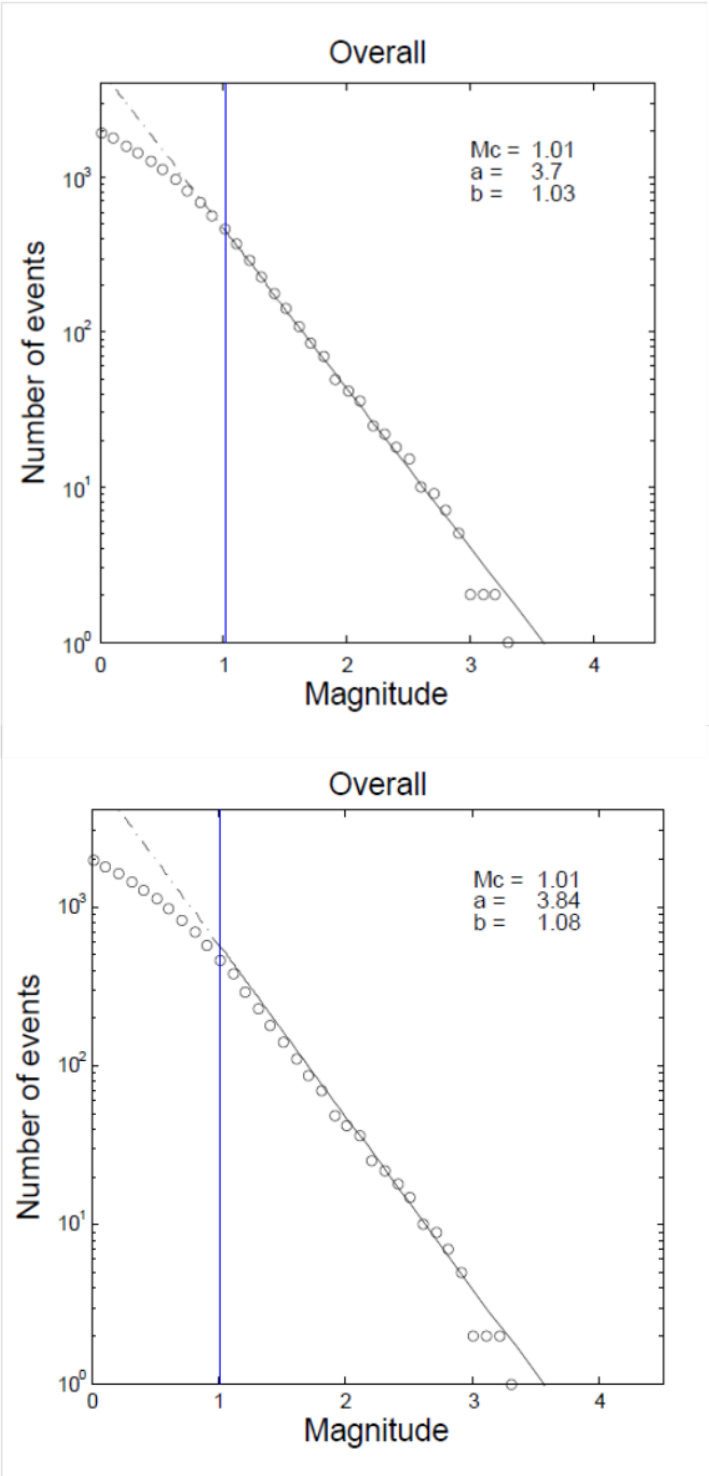

Figure 11: Overall *b*-value of the megathrust interface of Nicoya calculated by MLE (top) and LSR (bottom). Blue lines mark the *Mc*

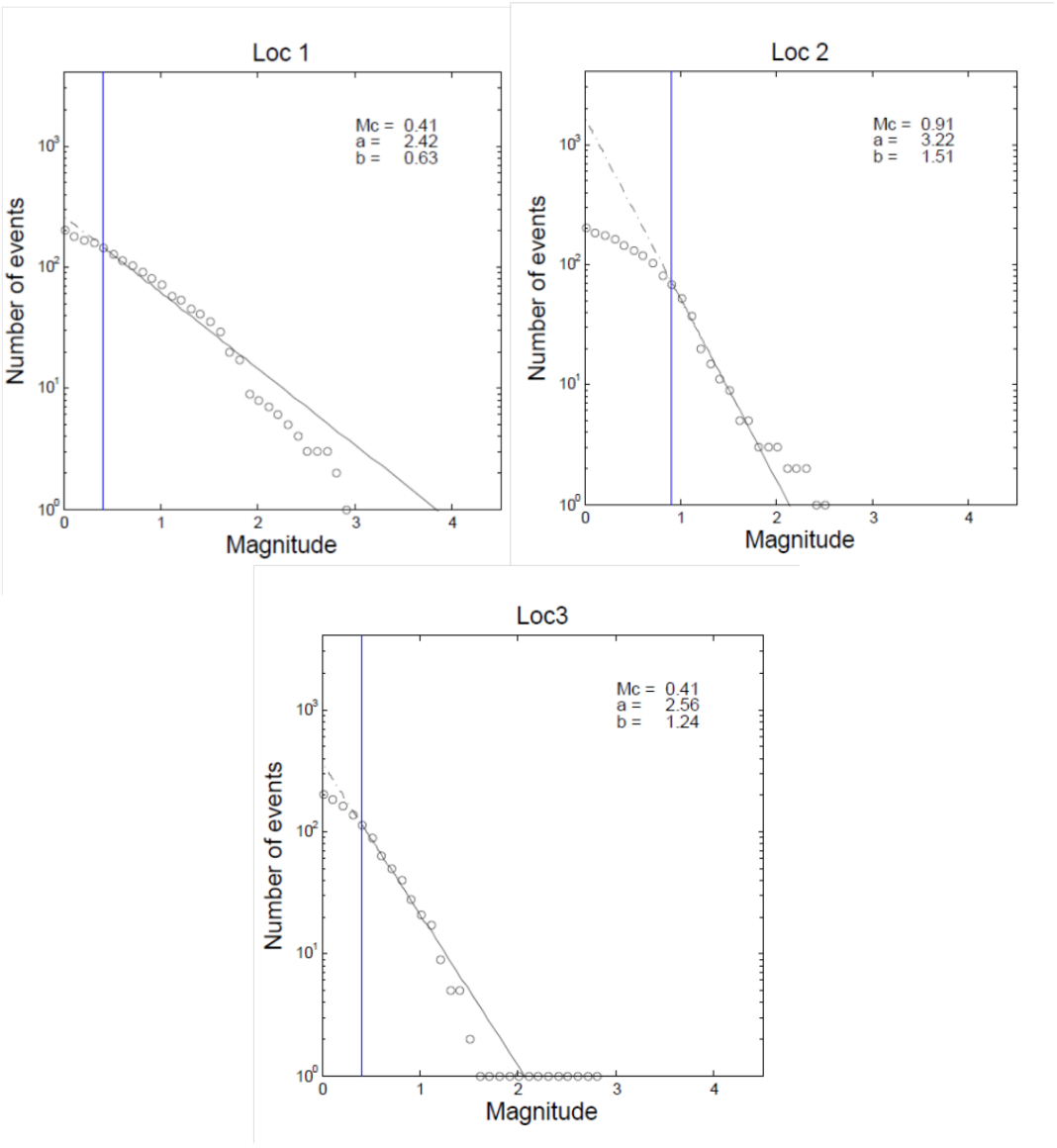

Figure 12: The *b*-values of the Nicoya megathrust interface on location 1, 2, and 3 denoted in Figure 5. They are calculated by MLE using sub-catalog that only contains the nearest 200 events. Blue lines mark the *Mc*

that occurred within the interface slab, which could exclude the influence of seismic activity that might not be directly related to the shear stress on the megathrust fault. In order to prove this point, I performed a test of plotting the spatial FMD using a catalog that includes seismicity in and out of the slab. I will discuss it later.

Mc determines the sub-catalog that only includes the magnitude of the earthquakes used for performing the computation of FMD. Before calculating the *a*-, *b*-values, and relevant errors, *Mc* for each of the one grid node was individually determined by the MCM and goodness of fit method. In Figure 13, *Mc* varies from 0.01 to 1.21. It is very interesting that the lowest *Mc* is almost equal to 0. This might attribute to the high sensitivity of seismic instrument, excellent geometry and locations of instrument deployment, and match-filtered technique for detecting small events. The lowest *Mc* is distributed along the central Nicoya and offshore, and the southeast Nicoya offshore. The highest *Mc* covers the northwest corner of Nicoya and also cuts through the southeast area.

Here, the *b*-value maps that are respectively generated by MLE and LSR (Figure 14 and 16). For the results computed by MLE, the spatial distribution of the *b*-value varies from 0.5 to 2.0 (Figure 14). The bootstrapping statistical method is applied in the process of calculating the *b*-value by using MLE. For each grid node, bootstrap of randomly selected earthquakes creates 10,000 subset catalogs from the existing subset to calculate the *b*-values by MLE algorithm, and the standard deviations of 10,000 *b*-values are also given in Figure 15. The standard errors of *b*-values are in the range between 0.02 and 0.44. The process of randomly sampling in the same subset catalog reliably estimates the error. Furthermore, the errors are less than 26% of the associated *b*-values in the interested region.

Similarly, I also make the FMD map (Figure 16) by applying LSR. In this case, the *b*-values vary from 0.63 to 2.1, which are relatively higher than the results of MLE. The standard deviation of *b*-value (Figure 17) varies from 0.03 to 0.38. However, the ratio

between the error and the associated *b*-value fluctuates from 2% to 46%. This result is higher than the standard error by MLE. Compared between the two *b*-value maps, the most obvious difference is that the results from the LSR are higher in the southeast offshore region. However, we still can see the similar pattern of FMD. Especially, the northwest part of Nicoya is covered with low *b*-values (~0.7), and a long narrow region near the central Nicoya is characterized with high *b*-values (~1.5). Figure 18 shows the sampling radius distribution when searching the nearest 200 events for creating subset catalog.

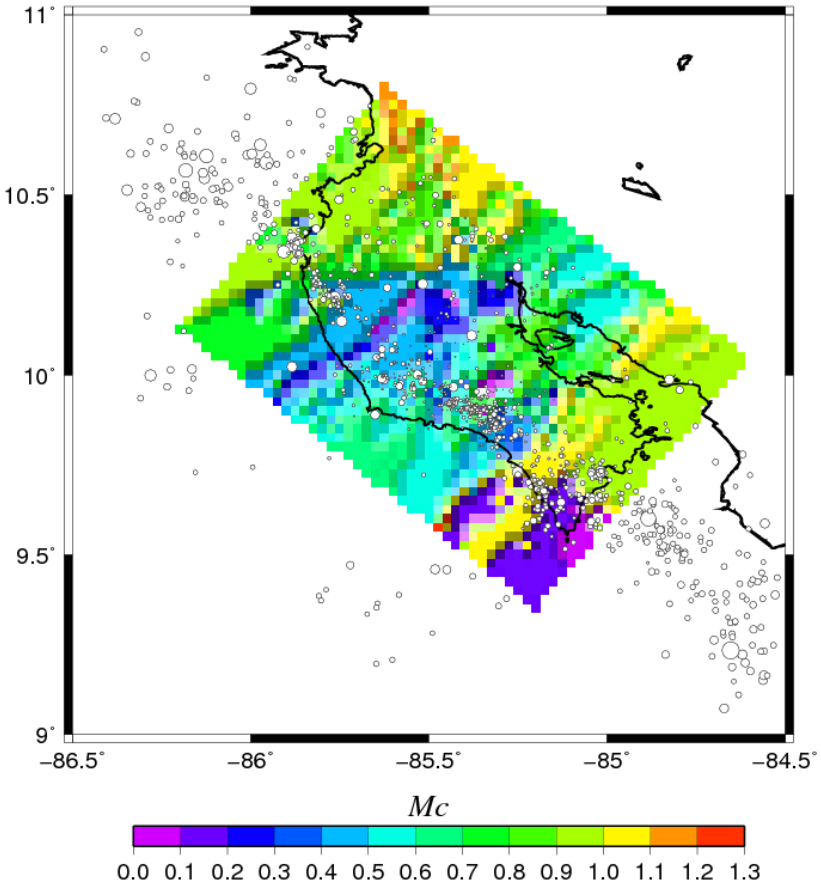

Figure 13: The distribution of *Mc* computed by the MCM and goodness of fit method. Black circles show the locations of earthquake within the interface. Only circles in the color region are used for the calculation.

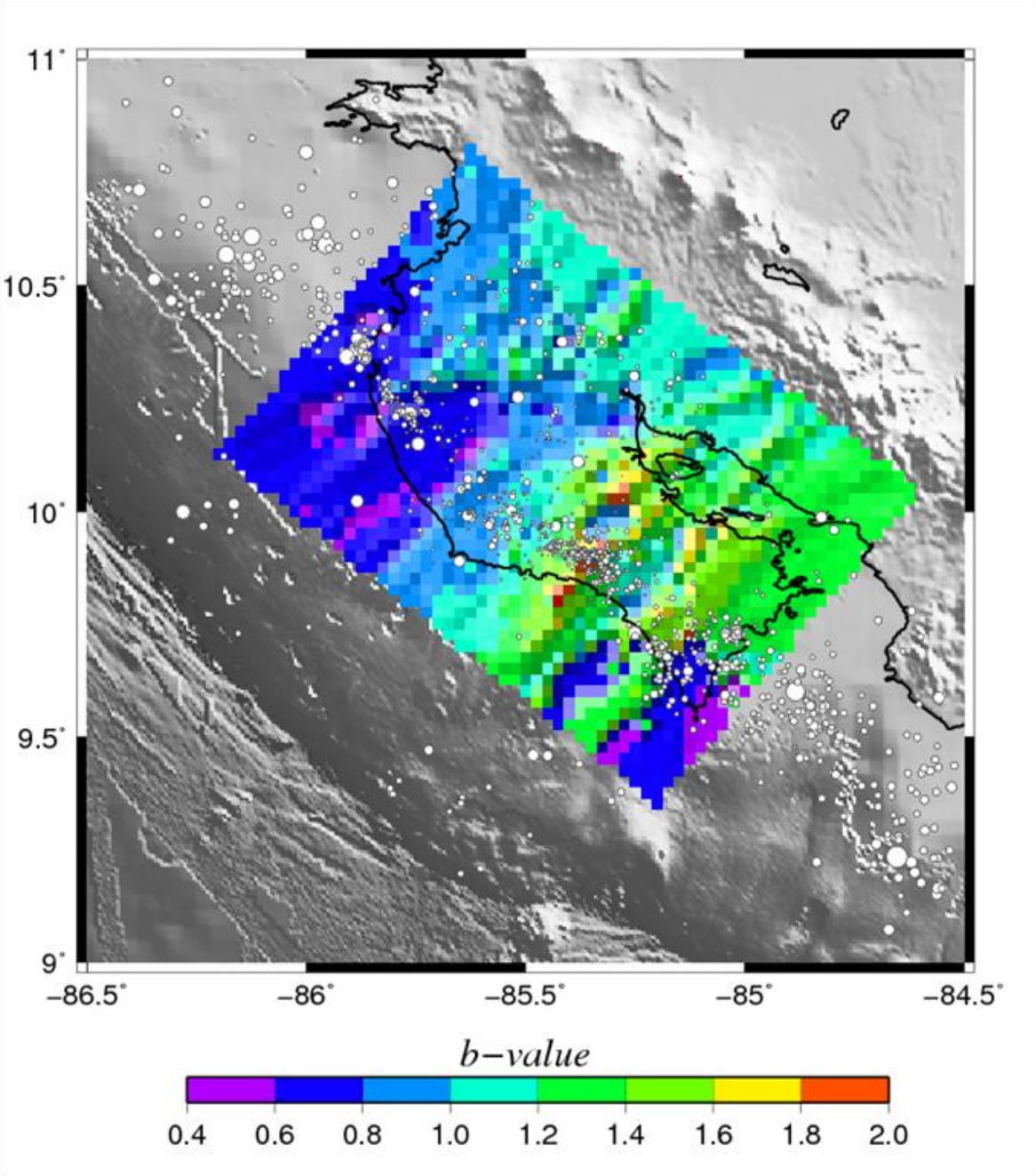

Figure 14: Spatial variation of *b*-values by using MLE with *Mc* from Figure 13.

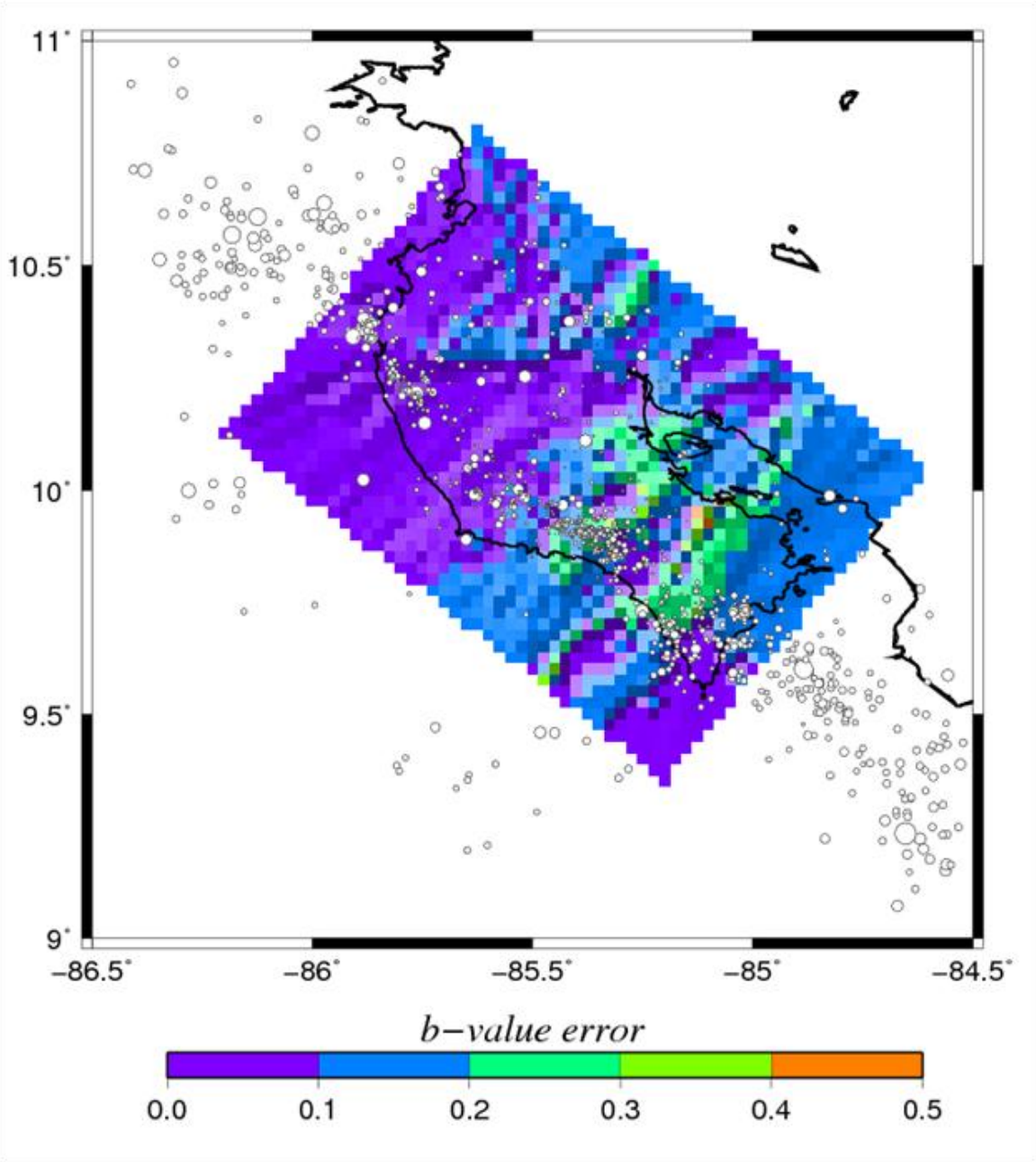

Figure 15: Spatial distribution of *b*-value errors that is determined by MLE using bootstrap method.

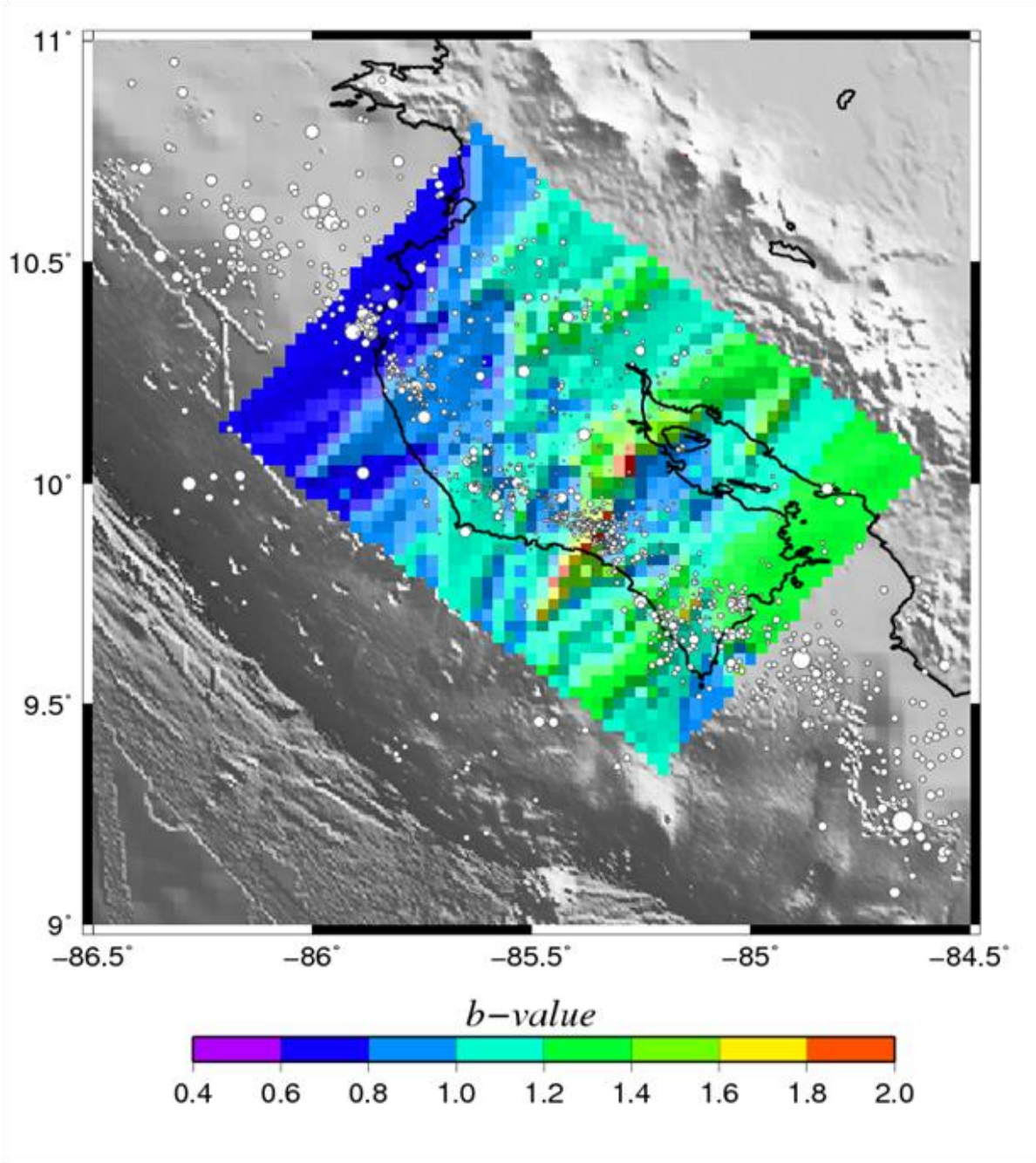

Figure 16: Spatial variations of *b*-values by using LSR with *Mc* from Figure 13. Circles are earthquakes within the slab.

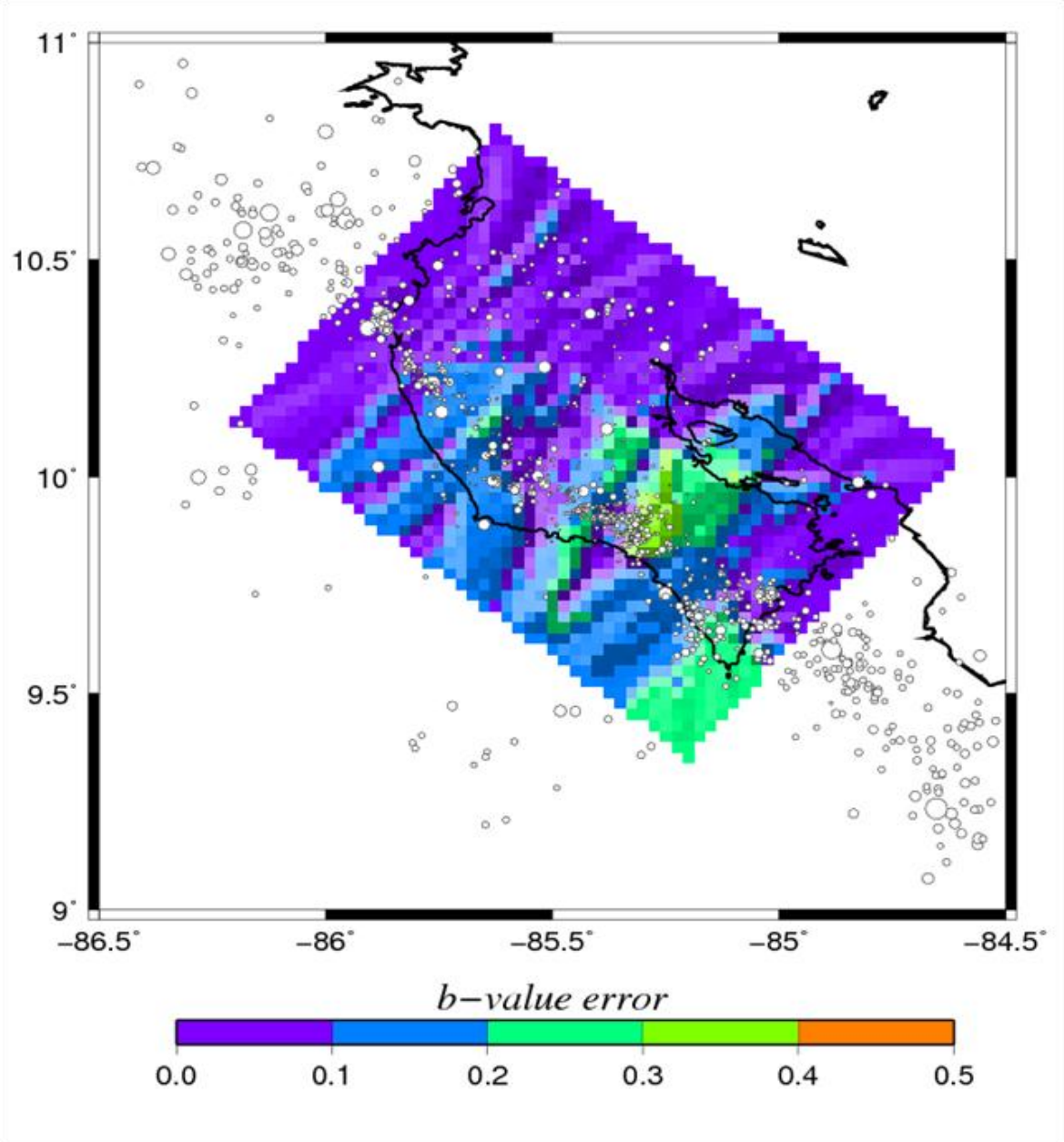

Figure 17: Spatial distribution of *b*-value errors that is determined by LSR.

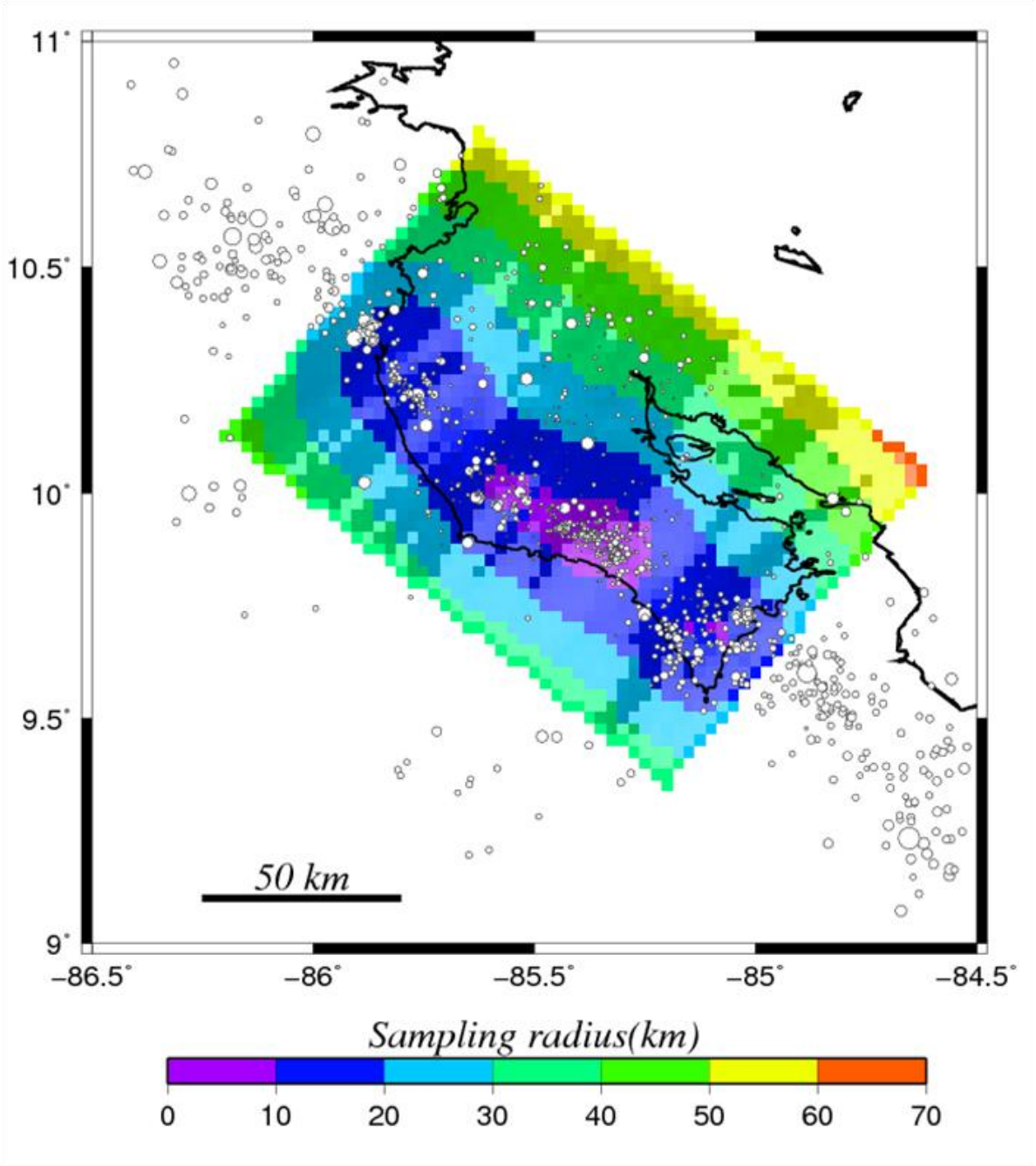

Figure 18: Spatial distribution of sampling radii for each node. Circles are earthquakes within the slab.

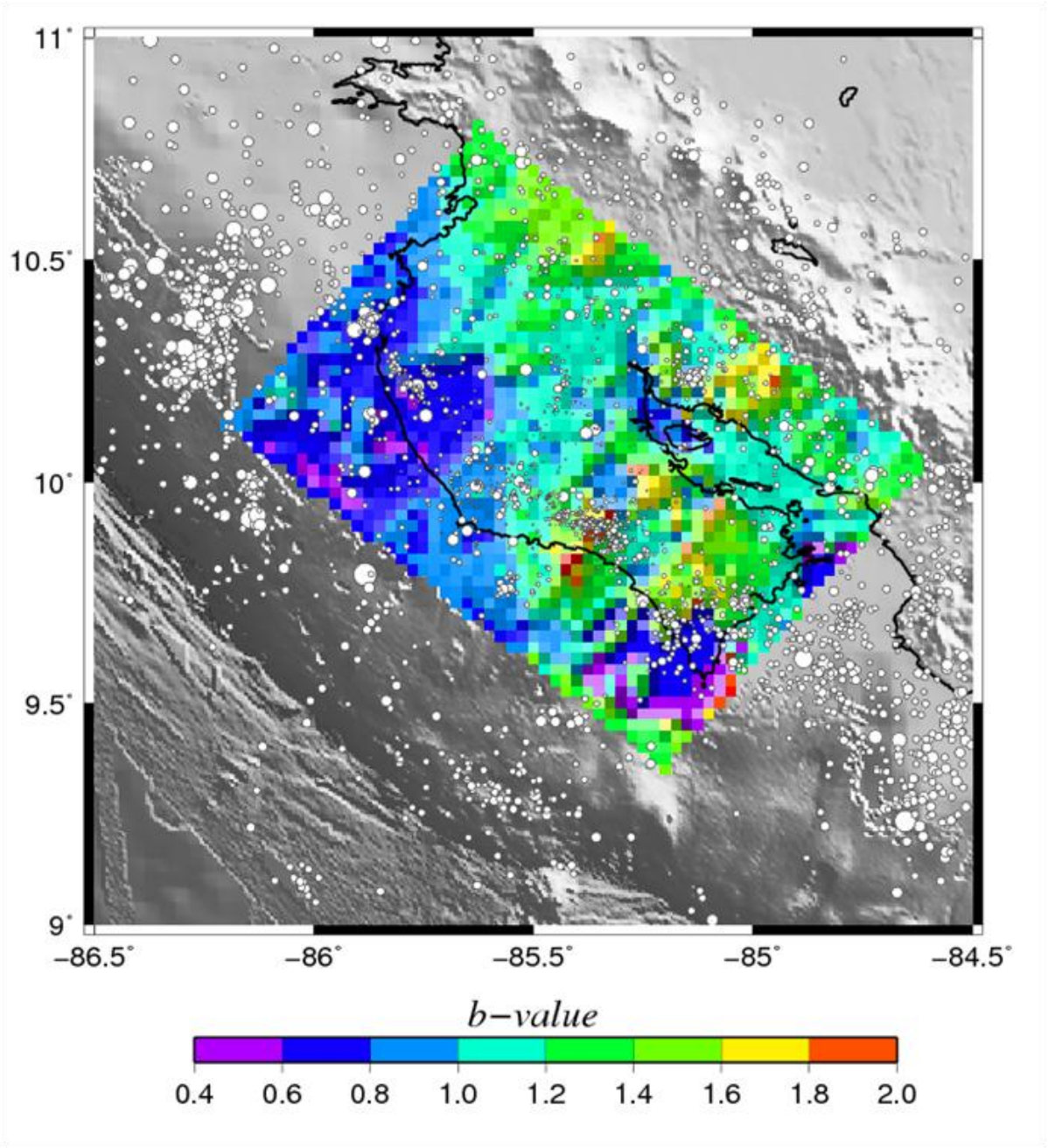

Figure 19: Spatial distribution of *b*-values using MLE and the catalog containing earthquakes in and out of the slab.

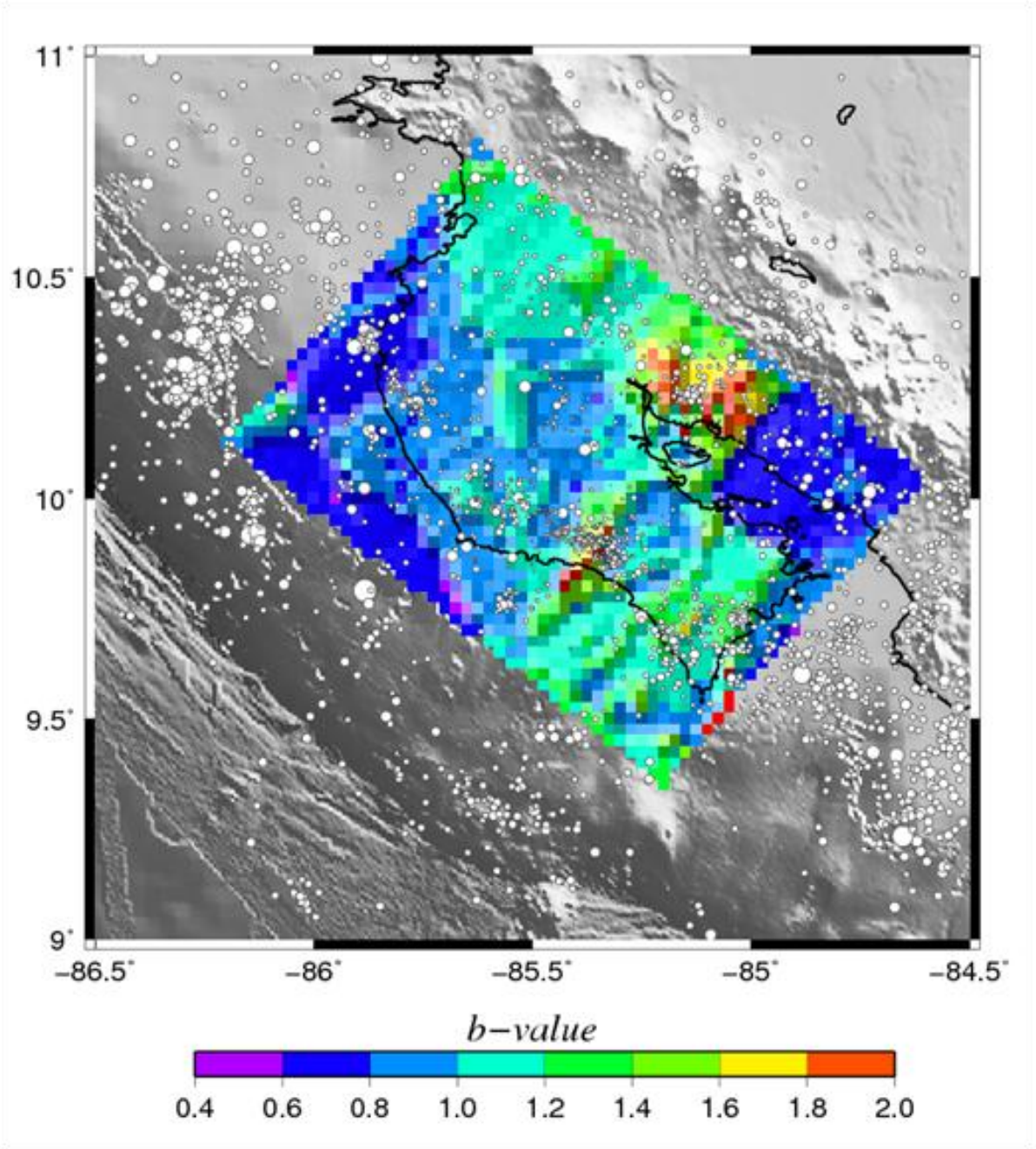

Figure 20: Spatial distribution of *b*-values using LSR and the catalog containing earthquakes in and out of the slab.

In this thesis, the sampling radius range beneath and near Nicoya is between 4 km and 66.5 km. For the major part of Nicoya, the sampling radius is less than 30 km. The region close to the coastline even has lower sampling radius, which is less than 20 km. It indicates that the FMD map covering the inshore area close to the coastline can more precisely reflect the FMD for each of one the grid node.

In order to verify whether the fitting parabolic boundaries of slab have the function of eliminating the influence of earthquakes that are not directly related to the subduction interface, I applied MLE (Figure 19) and LSR (Figure 20) algorithm to plot two FMD maps by using the whole catalog without setting the slab boundary. It is interesting that the overall *b*-values using MLE and LSR are 0.87+/-0.017 and 0.75+/-0.14, respectively. These results are more close to the global *b*-value of the subduction zone, which is between 0.5 and 0.8 [*Bayrak et al.*, 2002]. In detail, larger areas are covered with high *b*-values using MLE in Figure 19, especially the northeast side of Nicoya, which is close to the mainland of Costa Rica. For the LSR method in Figure 20, there are two patches that change significantly. They are both on the east side of Nicoya peninsula. One of them has higher values (~0.6) compared with Figure 16; on the contrary, and the other patch has lower *b*-values (~0.5) than the original values computed by using seismicity in the slab. Therefore, it shows that using earthquakes in the slab plays a role in eliminating the contamination of crustal or deep earthquakes.

3.4 Discussion

In this thesis, the major difference between the FMD generated by MLE and the one calculated by LSR is obviously shown at the southernmost corner of Nicoya. In

Figure 16, a *b*-value map using LSR has the value of ~1 at the southernmost tip of the peninsula. On the contrary, the same region in Figure 14 is characterized with a *b*-value of ~0.6 after applying MLE. Statistically, MLE relies on the numbers of events with magnitude between the mean magnitude and *Mc*, which are on the scale of 10 to 100 for each grid. When the magnitude goes higher than the mean magnitude, the event number drops to less than 10, which are not statistically large enough. However, LSR still puts similar weight on the one-digit number as two- and three-digit numbers. This may cause some bias. Thus, MLE is more widely used to calculate the *b*-value nowadays. However, the case in my thesis might be different. It is noticeable that the *Mc* (Figure 13) at the southern tip of Nicoya is even less than 0.2. I specifically examined this region on how these two different methods determine *b*-values. I sample the cell with a center coordinate of (85.25 ℃W, 9.5 ℃N). Figure 21 displays the results of *b*-value determination before and after applying the matched filter detection using LSR and MLE, respectively. It is interesting that *b* does not vary too much even using two different statistical methods before using the detection technique. However, the variation of *b*-value reaches up to 0.5 by using MLE and LSR after applying the detection technique. Based on the results, we can see that the events with magnitude between 0.5 and 1.2 produces the bulgy shape on the *b*-value slope figure. The activities with magnitude less than 0.3 may cause the bias of the *b*-value. The explanation for this case might be that the matched filter method not only detects some real earthquakes but also brings in noise information to the catalog. To verify this assumption, I still use the node of (85.25 ℃W, 9.5 ℃N) and 200 events within its local subset catalog to map out the spatial and temporal distribution of events (Figure 22) with magnitude less than 0.3. Figure 22 (a), (b), and (c) show the spatial locations of

those small events in three dimensions. There is no obvious cluster for the small events, which share the similar distribution pattern of other earthquakes in the same local subset catalog. Figure 22 (d) shows the temporal distribution of these small activities. Still, no obvious cluster is shown in the temporal distribution. The spatial and temporal distribution of these small events cannot prove that these activities with magnitude less than 0.3 are associated with swarm activities, aftershocks or slow slip events. I also specifically examined the waveforms of one of these detected small events (Figure 23). The detected small earthquake (magnitude of 0.27) occurred at 22:49:00 on March 1st 2009. Unfortunately, I did not observe any earthquake-shape waveforms within this period of time after applying the 3-8 Hz filter. We can suspect that these micro-earthquakes might likely be associated with the matched filter detection algorithm that I applied in this case. In addition, LSR is more stable on determining *b*-values in this case due to the even dependence among the numbers of large events and small events. Thus, the results derived from LSR are used in further discussion.

It is obvious that the *b*-values are spatially variable (Figure 16) along the subducting interface of Nicoya. The pronounced regions with the lowest *b*-value (~0.6) appear on the northwest side of Nicoya peninsula and the offshore. The minor region in the southern coastal area of the peninsula offshore is also characterized with low *b*-values (~0.9). In contrast, the highest *b*-value (~2) covers the southeast part of Nicoya, where CNS plate subducts. Half the area of the southern Nicoya is covered by high *b*-values (>1.2). As discussed in chapter 3.1, the *b*-value can be used as a stress meter to reflect the stress regime along the fault. Generally, the lower *b*-value means higher stress, and the higher *b*-value indicates lower stress. In another words, highly accumulated stress is

along the fault right beneath the northern part of Nicoya. The more stress accumulated along the fault, the more coupling degree would exist. After the megathrust interface cannot bear the highly accumulated stress anymore, rupture initiates and bursts into a large earthquake. On the contrary, the cumulative stress begins to drop off beneath Nicoya where EPR transits to CNS. The CNS crust under the Nicoya may be experiencing low stress accumulation.

Newman et al. [2002] inferred that the up-dip limit of seismogenic interface under the northern Nicoya Peninsula is 10 km deeper than the southern side. *Deshon et al.* [2006] also proved that the width of seismogenic zone under EPR plate could reach up from 70-75 km to 100 km off the trench. Even though the low *b*-value region under the northwest Nicoya is fairly far away from the trench, it is still in the seismogenic zone. Thus, it is possible that highly accumulated stress appears on this side. Due to the large sampling radii, roughly about 30 to 40km (Figure 18), the low *b*-values might be affected by the seismicity near the coastline for the offshore region of west Nicoya. Thus, the FMD of offshore region of the west Nicoya might not be accurate enough to present the local *b*-values for each individual cell. *Thomas et al.,* [2007] derived a subduction interface of three-dimensional geometry for the Nicoya area using interplate seismicity. It is interesting that this model reveals a topographical transition from the EPR crust to CNS crust (Figure 24). *Carena* [2011] proposed that the thrust lateral ramps might have high potentiality to be considered as sources of megathrust earthquakes. This idea supports that the interface beneath central Nicoya, where the EPR crust transits to CNS crust, is characterized with stress concentration and coupling. On the east side of offshore Nicoya, Fisher seamounts (Figure 25) create an environment of asperity on the interface,

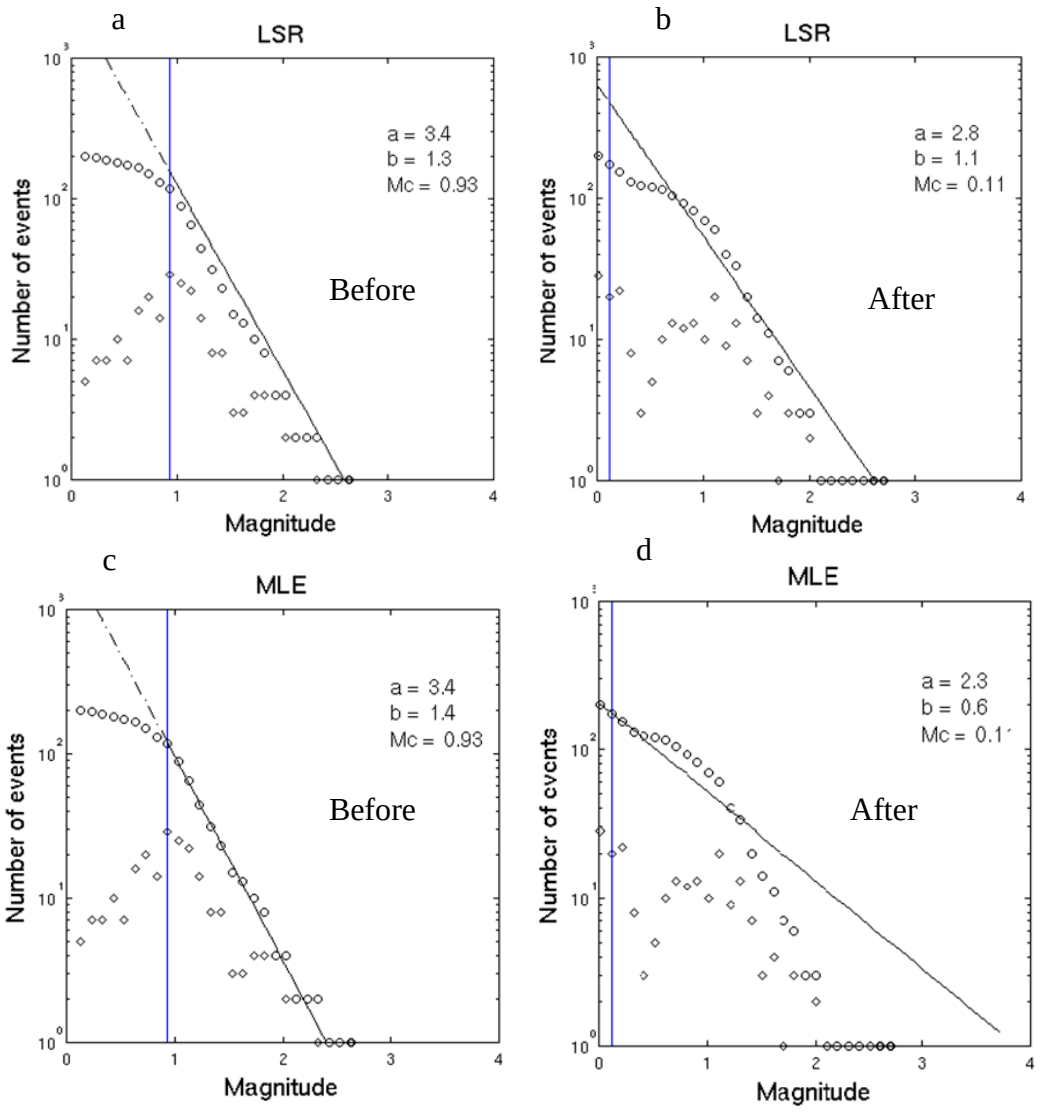

Figure 21: The *b*-values of (85.25 ℃W, 9.5 ℃N) on the Nicoya megathrust interface using LSR and MLE before and after applying matched filter technique. The figures on the left side display the b-values determined by the old catalogue using LSR (a) and MLE (c). The figures on the right side show the *b*-values after applying the matched filter method using LSR (b) and MLE (d). Circles denote cumulative numbers of events, and diamonds denote non-cumulative numbers of events.

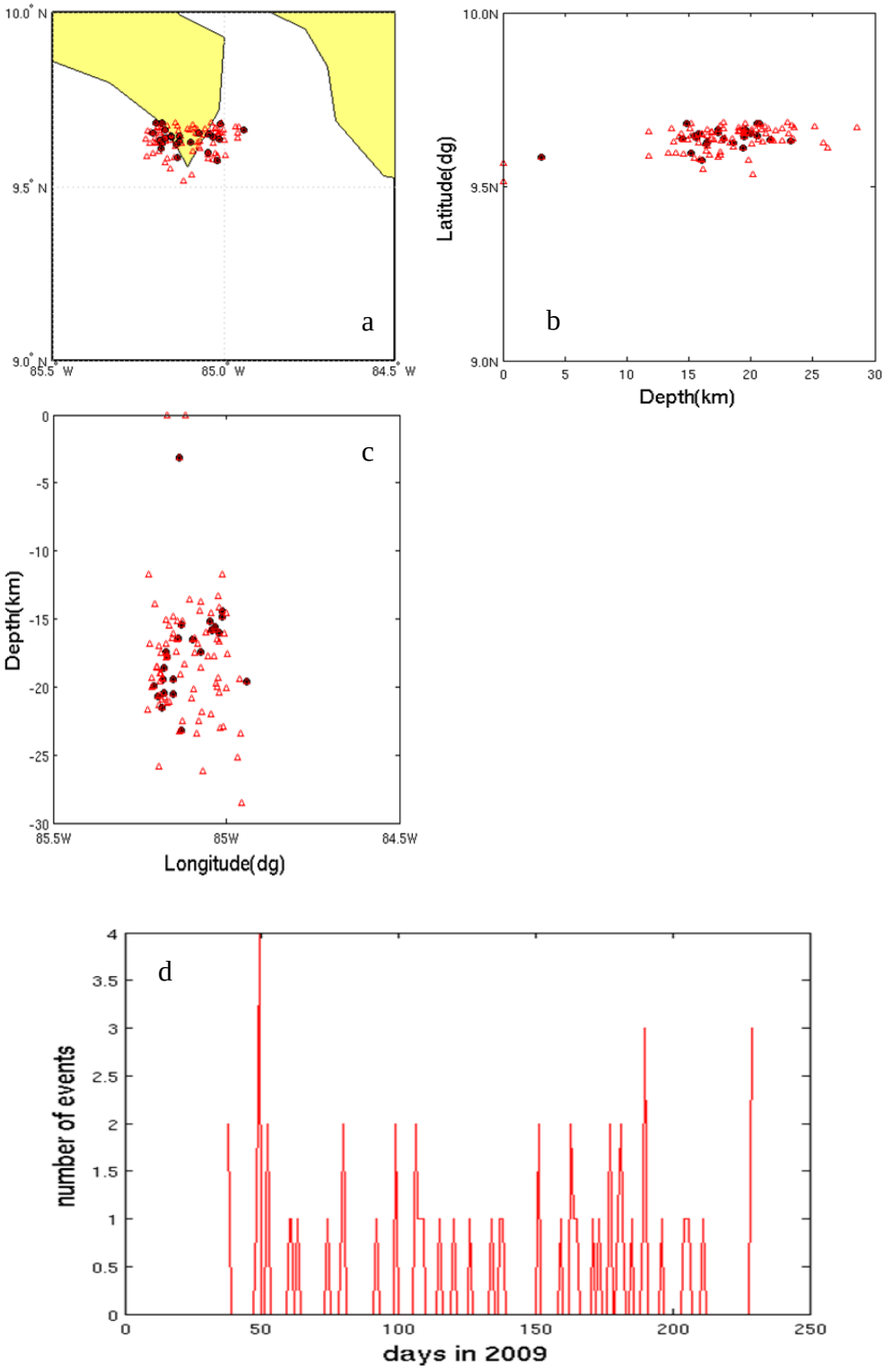

Figure 22: The spatial (a,b,c) and temporal (d) distribution of earthquakes in the local subset catalog of node (85.25 ℃W, 9.5 ℃N), which locates at the southernmost tip of Nicoya. Red triangles represent earthquakes with magnitude larger than 0.3, and solid black circles are the small earthquakes (M_L<0.3)

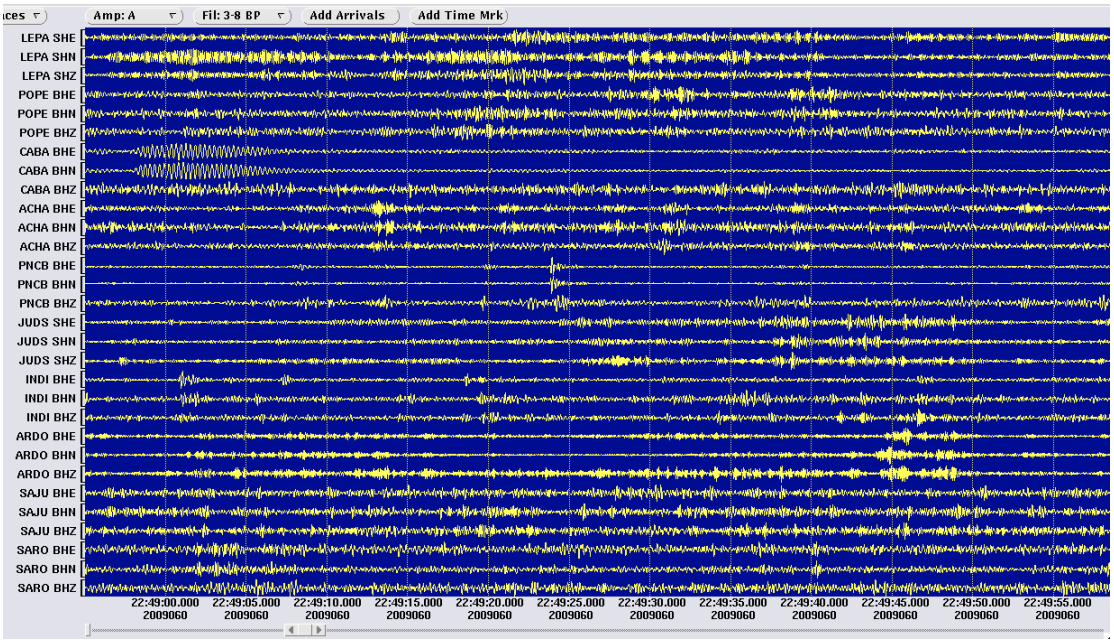

Figure 23: The waveforms of detected "event" that occurred at 22:49:00 on March 1st 2009. The waveforms are filtered by 3-8 Hz. The results are shown in Antelope 4.11.

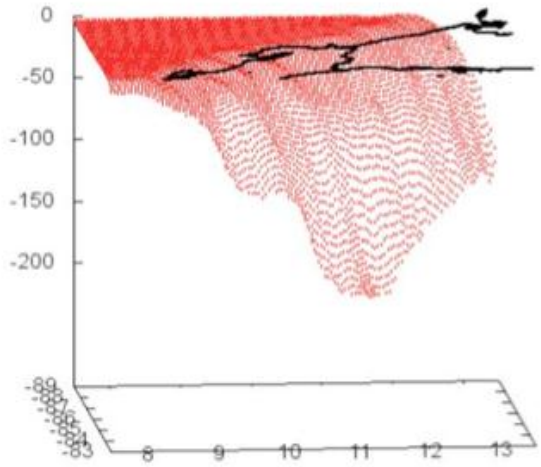

Figure 24: The three-dimensional subduction interface near and under the Nicoya region. Z-axis is the depth in km, X-axis is the latitude in degree, and Y-axis is the longitude in degree. *
Referenced from: http://geophysics.eas.gatech.edu/anewman/MAT/.

which may cause stress concentration on the fault too. Using a seismic velocity model, *Husen et al*., [2003] inferred a subducted seamount beneath Nicoya along the direction of Fisher seamounts with a distance of 40 to 80 km away from the trench. The narrow band

of the low *b*-values (0.8~0.9) on the southeast corner in Figure 25 coincidentally covers the subducted seamounts on the map in a horizontal view. This phenomenon also supports the idea that asperity can produce stress concentration and interface locking as well.

The stress regime that uses FMD as a proxy in this study are not only supported by the topographical and seismic data, but also supported by the degree of locking and the fault slip of slow slip event that are both derived from geodetic models. As previously mentioned in chapter 1.3, *Feng et al.* [2010] performed an inversion model of surface displacement recorded by GPS data from 1996 to 2010 to infer the slip distribution (Figure 25) along the megathrust fault under Nicoya. They found three patches that have been fully locked. The result is similar to the one derived by *LaFemina et al.* [2009], who used the geodetic model by combining the episodic and continuous GPS data from 1993 to 2005. These three locked patches coincidentally cover the low *b*-value areas in this study, except that a relatively small region characterized with high *b*-value near the central Nicoya is still covered with locked portion. On the contrary, the locking percentage, which is less than 20% in the southeast corner of Nicoya, is characterized with high *b*-values, which means low stress accumulation on the fault. In addition, *Outerbridge et al.* [2010] also performed an inversion model of continuous GPS data across the Nicoya Peninsula that was recorded in 2007. They detected a slow slip event (SSE) occurred under the Nicoya beginning in May 2007, lasting about 40 days. Conceptually, SSE is the continuous and silent fault movement that is opposite to the subducting direction of the downgoing plate in the environment of subduction zone. Usually this phenomenon goes so slowly and silently that it cannot be detected by

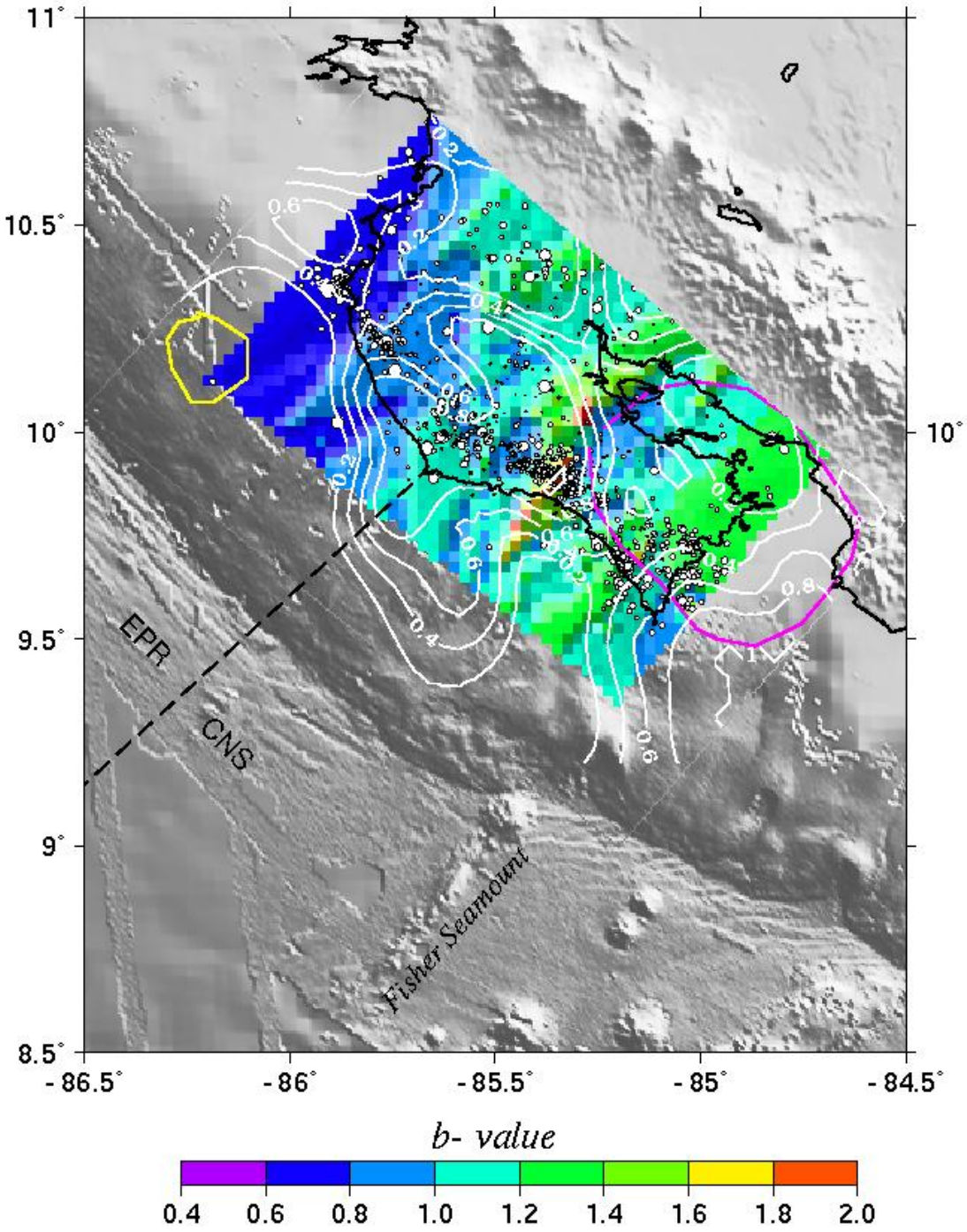

Figure 25: Comparison of spatial distribution of *b*-value using LSR and interface locking derived by geodetic model [*Feng et al.*, 2010]. The white contour lines are the normalized locking on the fault. The purple contour line defines the patch of 2007 slow slip event (SSE) with the maximum slip of 12 cm that centered at 25-30 km depth. The yellow contour line defines the other patch of 2007 SSE with the maximum slip of 5cm at 6km depth [*Outerbridge, et al.*, 2010].

seismometers in certain areas. However, continuous GPS data can take the advantage of continuously recording the surface displacement to capture the weak variations, which might have influence on the evolution of subduction environment. It is interesting that *Outerbridge et al*. [2010] detected two patches of slip under or near the Nicoya. One of them occurred at a shallower depth of 6km with the maximum slip of 5cm near the seismogenic zone up- dip of EPR crust near the Nicoya offshore; the other patch located at a depth of 25-30 km with the maximum slip of 12cm underneath southeast Nicoya (Figure 25). These two patches of slip overlap the free locked portions that were derived by *Feng et al*. [2010] and *LaFemina et al* [2009]. It can be interpreted that the SSE may release the cumulative stress on these free locking portions of fault. However, the shallower patch of SSE is still in the zone of low *b*-values. It might be explained by the fact that timing and errors of matched filter technique may cause the bias. In addition, it is also possible that 5cm slip did not release much stress cumulated along the fault. Moreover, the sampling radius of FMD in that region is approximately about 40 km; hence, this low *b*-value zone of northwest Nicoya offshore might be smeared by the *b*-values of inland region. Significantly, the larger slip patch corresponds to a high *b*-value region, which indicates low stress accumulation. However, the inversion model of GPS data is modestly dependent on the geometry of subducting plate interface. The simplicity of fault geometry might cause the bias of fault locking. Due to the wide range of seismicity selection within the slab, this study is not greatly dependent on the fault. Hence, it is less likely that FMD and locking contour lines can be perfectly matched up.

In order to verify if the spatial distribution of *b*-values has temporal changes, I also examined the difference between my result with the one generated by *Ghosh et al*.

[2008], who used similar procedure and MLE with the seismic catalog between late-1999 and mid-2001 in the same area. According to their results (Figure 26), they interpreted that the fault beneath the central Nicoya is characterized with increased stress, which means high locking. On the other hand, the regions on the two sides of Nicoya suggested weak coupling along the interface. The most striking variation between our and their results is that the *b*-values of my results on the northwest side of Nicoya are less (~1.2) than their results. It is interesting that the central Nicoya and offshore does not change too

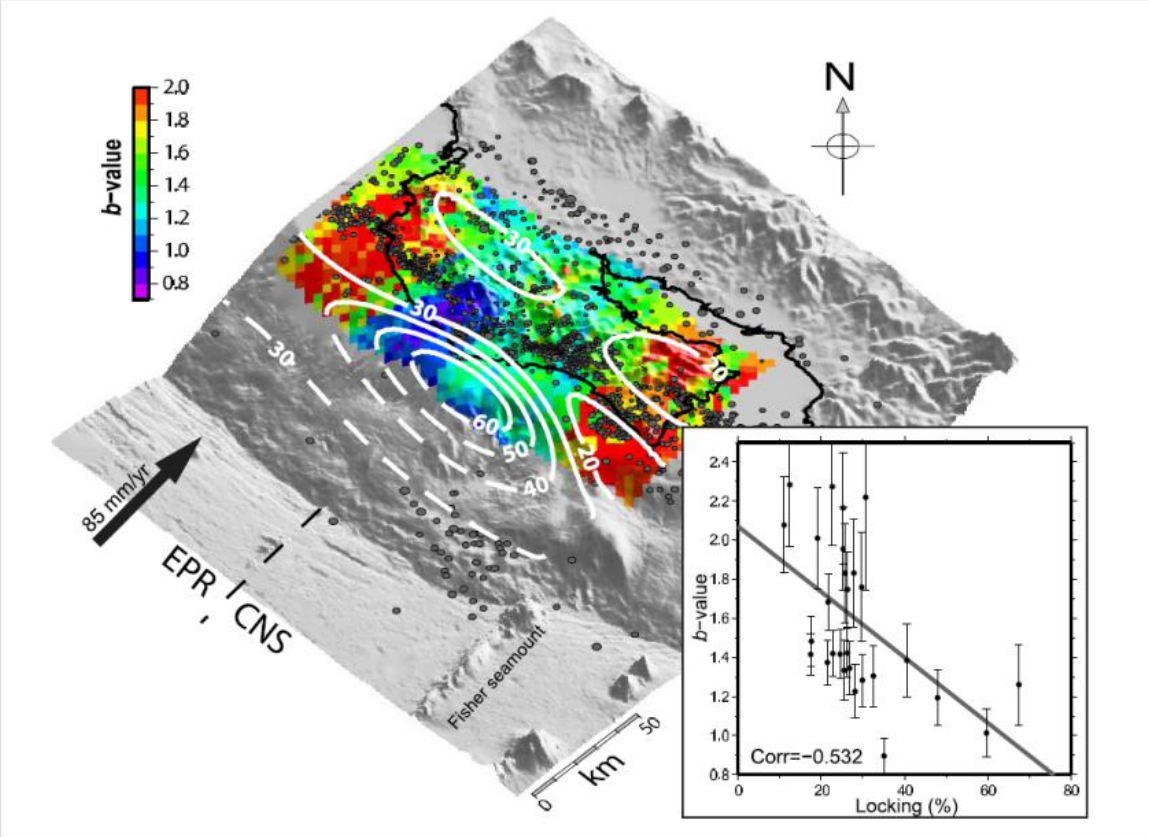

Figure 26: *b*-value map of Nicoya using MLE and seismic data recorded between late 1999 and mid-2001. [Ghosh *et al*., 2008]. White contours are the locking degree derived from geodetic model by *Norabuena et al*. [2004]. Inset is the comparison of *b* and locking.

a

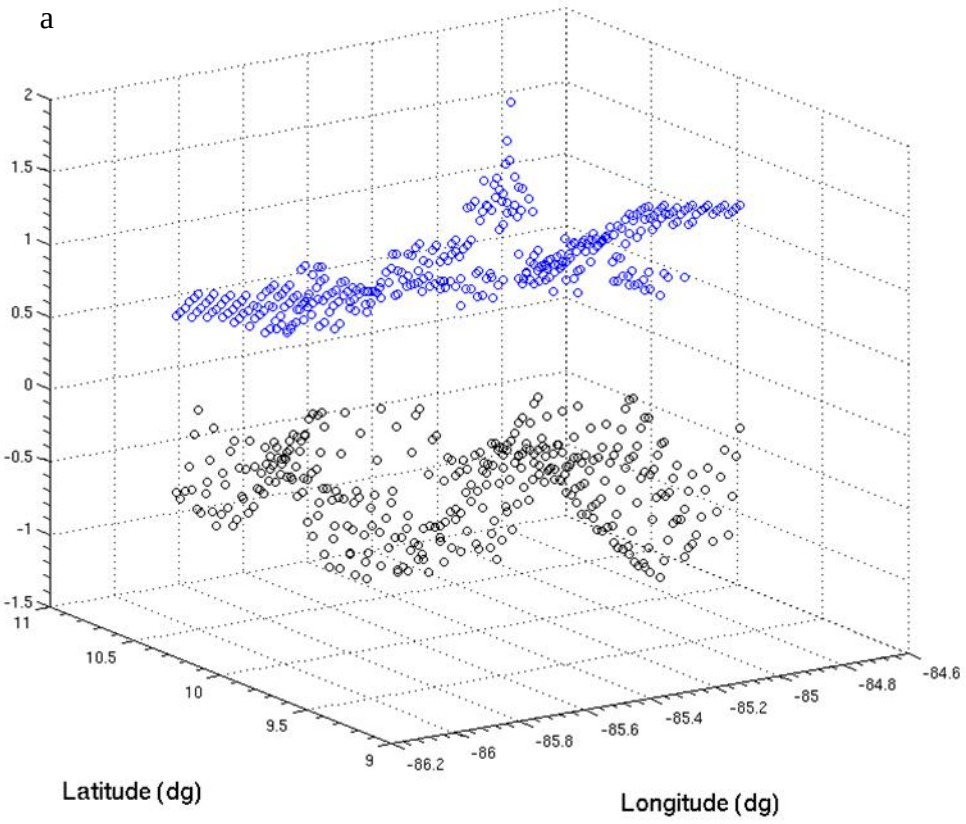
2
1.5
1
0.5
0
-0.5
-1
-1.5
11
10.5
10
9.5
9
Latitude (dg)
-86.2
-86
-85.8
-85.6
-85.4
-85.2
-85
-84.8
-84.6
Longitude (dg)

b

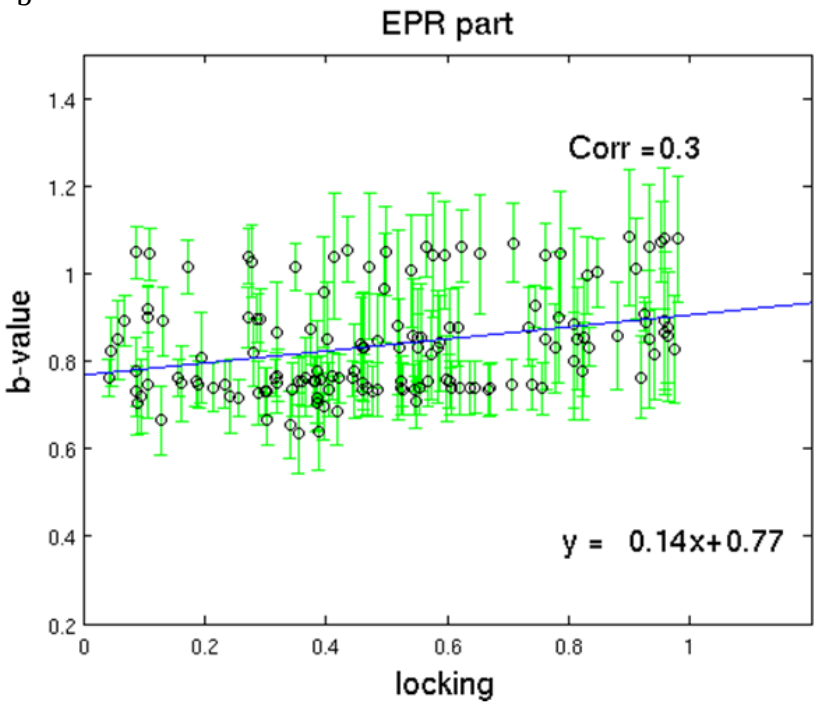
EPR part
Corr = 0.3
y = 0.14x+0.77
b-value
locking
1.4
1.2
1
0.8
0.6
0.4
0.2
0
0.2
0.4
0.6
0.8
1

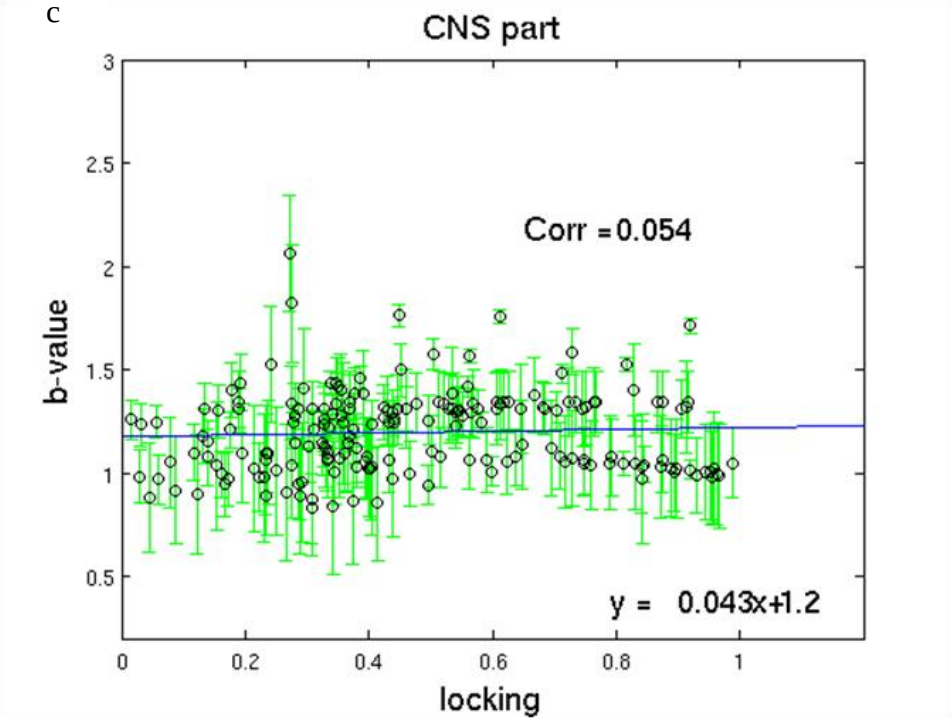

Figure 27: (a). Comparison between the *b*-values (after applying the matched filter technique to the seismicity in the slab) in LSR and negative value of the normalized GPS locking beneath Nicoya. The blue circles represent the *b*-values plotted on the grids, and vertical axis denotes corresponding values. Similarly, the black circles are locking degrees. The vertical axis denotes the negative values of corresponding locking degrees. (b) and (c) show the comparison between the normalized GPS locking and the *b*-values in LSR underneath EPR and CNS, respectively. Blue lines show the best fit using least square method. Corresponding correlation values and fitting equations are given as well.

much. It is still characterized with *b*-values less than 0.8, which means this region is still experiencing high stress accumulation. There might be several reasons to produce the variation. (a), the seismometers installed on Nicoya are generally more sensitive than the ones 9 years ago. Some instruments with sampling rates of 20 and 40 have been updated to 50. (b), The matched filter technique also helped us find more events in 2009. At the same time, it also brought noise data into the catalog. (c), The algorithm of determining

local magnitude is also different. Antelope 4.11 has updated a new algorithm for determining local magnitude, which might produce some variations. (d) The seismic data are collected in different periods of time. (e) The statistical method that I am using is also different from the one that they used. Combining with all these possible facts, it is hard to draw any reliable conclusion on why and how the FMD pattern changes in just 9 years. After all, we might need more reliable magnitudes from the catalog to obtain more reliable results for making further discussion and conclusion.

In order to verify how much the *b*-value can be correlated with the geodetic coupling degree, I also make a quantitative comparison between the *b*-values and the locking. The FMD that I am using is still derived from LSR, and the geodetic locking is from *Feng et al.* [2010]. To focus on the interface underneath Nicoya, only the nodes with a sampling rate less than 30 km will be used to compare. Interestingly, Figure 27 (a) can give us a general idea that the *b*-value and the locking percentage might be correlated. Here, the blue circles represent the *b*-values on the corresponding grid, and vertical axis denotes corresponding *b*-values. Similarly, the black circles are negative values of normalized coupling degree. The vertical axis denotes the negative values of corresponding coupling degree. There are two peaks on the locking plot. However, there is only one peak on the *b*-value plot. Coincidentally, the matching peaks of the *b*-values and locking are both on the CNS side beneath Nicoya Peninsula. Thus, I divide the figure into two parts, which correspond to EPR on the northwest side and CNS on the southeast side. However, the correlation coefficient for the EPR part is 0.3, which is not high; and the fitting line is $y=0.14x+0.77$. By testing 10,000 randomly generated data sets with the same sampling numbers, 146 for the EPR part, I found that 99.9% randomly generated

a

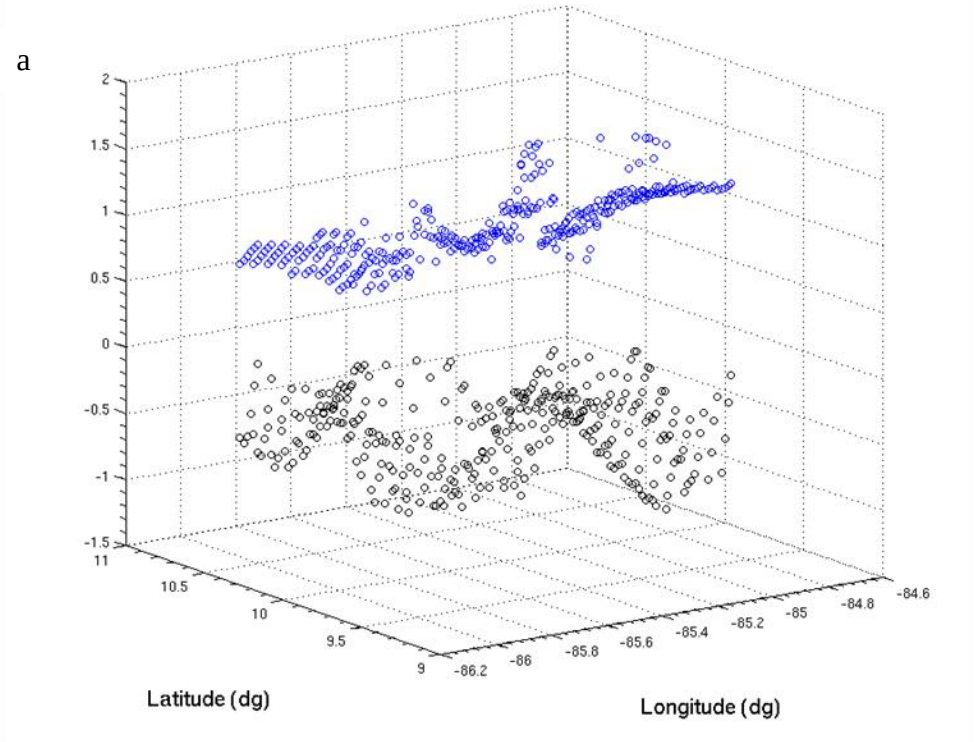
2
1.5
1
0.5
0
-0.5
-1
-1.5
11
10.5
10
9.5
9
Latitude (dg)
-86.2
-86
-85.8
-85.6
-85.4
-85.2
-85
-84.8
-84.6
Longitude (dg)

b

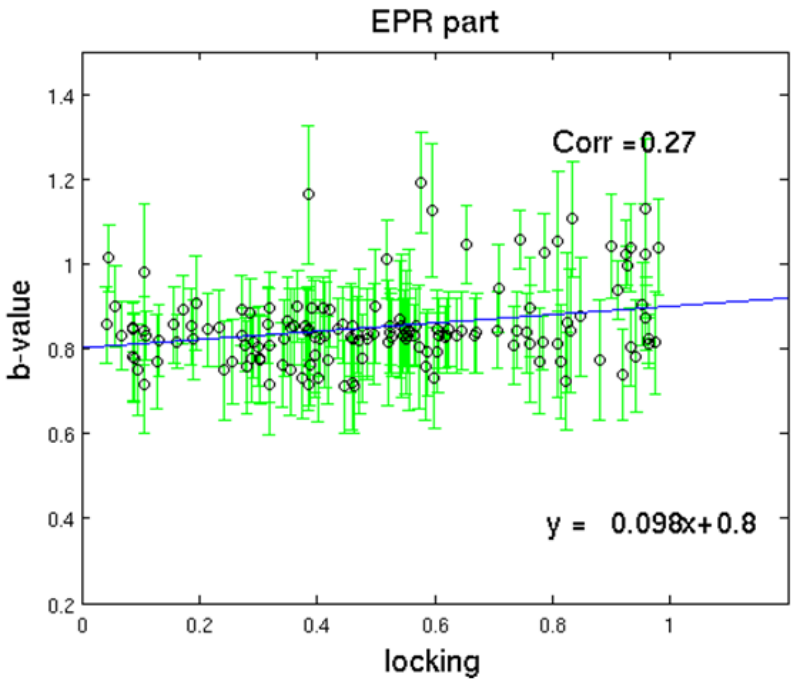
EPR part
Corr = 0.27
y = 0.098x+0.8
b-value
locking
1.4
1.2
1
0.8
0.6
0.4
0.2
0
0.2
0.4
0.6
0.8
1

c

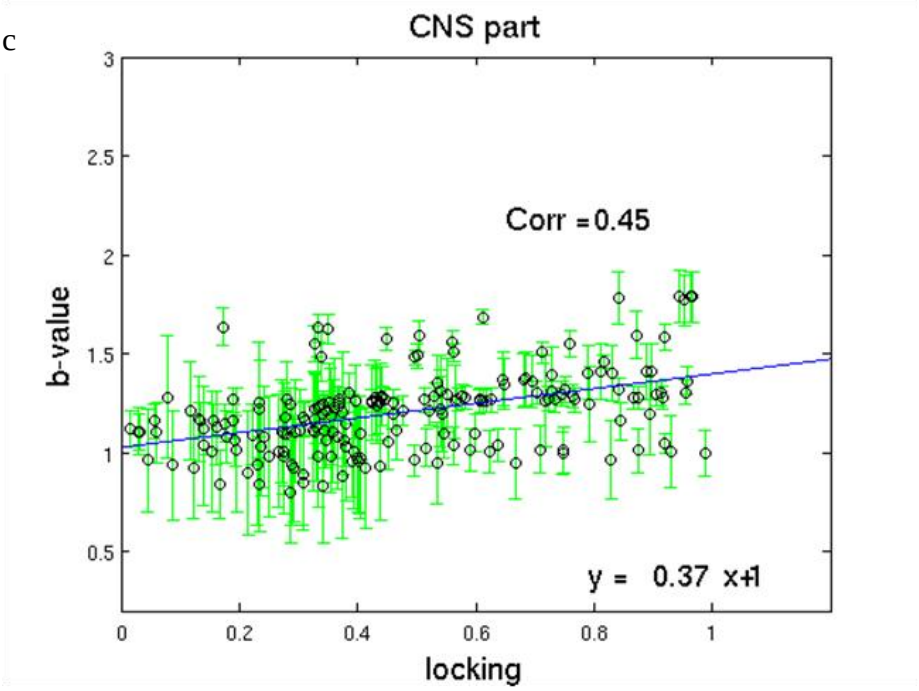

Figure 28: (a). Comparison between the *b*-values (before applying the matched filter technique to the seismicity in the slab) in LSR and negative value of the normalized GPS locking beneath Nicoya. (b) and (c) show the comparison between the normalized GPS locking and the *b*-values in LSR underneath EPR and CNS, respectively. The denotations are similar to the ones in Figure 27.

data sets do not have an absolute correlation larger than 0.3. For the CNS part, the correlation coefficient is only 0.054, and the fitting line equation is y=0.043x+1.2. Using the same sampling number of 191, the results of similar statistical test show that the possibility of absolute correlations (>0.054) from random data sets only can be excluded at 54.2% confidence. Considering the impact of noise data that are possibly brought by the new event detection method, I also make the similar graphs (Figure 28) as Figure 27 to show the relation between FMD (determined by LSR) and geodetic coupling before applying the detection method. The positive correlation of 0.45 is on the CNS part, and the equation of fitting line is y=0.37x+1. Using the sampling size of 191, the same

statistical test shows that 100% of the randomly generated data sets have absolute correlations smaller than 0.45. While the correlation value on the EPR part is 0.27, which is still relatively low. The equation of fitting line is y=0.098x+0.8. Using the sampling size of 146, the result of statistical test shows that 99.9% of the randomly generated data sets have absolute correlations smaller than 0.27. These results of positive correlation between FMD and coupling degree are different from the negative correlation that was derived by *Ghosh et al* [2008]. Still, there are several reasons for having these variations. 1). Different geodetic models generate different locking degrees; 2). Different statistical methods (LSR and MLE) and collected data in different time periods produce different FMD; 3). The detection algorithm may bring noise data into the catalog. Thus, we may not draw a quantitative conclusion on the relationship between *b*-values and locking derived by geodetic modeling at this point. We need to move further to obtain a catalog with more reliable magnitudes for drawing conclusion on the relation between FMD and geodetic coupling.

CHAPTER 4

CONCLUSIONS

In this thesis, more than 7,000 relocated earthquakes near and beneath the Nicoya Peninsula of Costa Rica were obtained by manual investigation. The catalog contains the earthquakes recorded from February to August 2009. I used the high SNR waveforms from the earthquakes that were beneath Nicoya as templates and detected more than 5,000 earthquakes using matched filter algorithm. Eventually, there are 4,347 qualified micro-earthquakes within the defined slab for plotting FMD on the top of Nicoya Peninsula, and more than 3,000 events were not listed in the original catalog.

The overall *b*-value for this region is 1.08+/-0.082, which is relatively lower than the globally average *b*-value (0.5~ 0.8). This might indicate the moderate coupling of megathrust interface under the Nicoya Peninsula of Costa Rica. The spatial distribution of *b*-values varies from 0.5 to 2.0, which suggests the variation of coupling along the fault underneath the Nicoya Peninsula. I also made the plots of FMD beneath Nicoya using all events without setting any slab boundary. The results are different from the ones only using earthquakes selected in the interface slab; and the overall *b*-value for this region drops to 0.75+/-0.14, which is close to the range of the globally average *b*-value (0.5~0.8) [*Bayrak et al*., 2002] in the subduction zone environment. This process proves that using earthquakes only in the slab can exclude the contamination of crust earthquakes and deeper earthquakes. It is observed that the northwest corner of Nicoya is characterized with low *b*-values. Due to the older age and the cooler temperature of the EPR plate than those of the CNS plate, the EPR crust beneath northwest Nicoya extends the seismogenic zone up to 100 km from the trench. It is still likely that high stress

accumulation can reach up to the region that is so far away from the trench. In addition, central Nicoya and the southernmost tip offshore region are also characterized with low *b*-values. The condition of rough topography at these two regions probably causes stress accumulated along the fault. On the other hand, the high *b*-value zone under the northeast side of Nicoya indicates low stress accumulation. For some part of FMD, the locking contour lines [*Feng et al.* 2010; *LaFemina, et al.* 2009] that are inverted from GPS data correspond well with it. The region of 2007 SSE with the maximum slip corresponds to the high *b*-value portion. It still suggests that stress might be less accumulated due to the release of stress in terms of SSEs. However, I did not find any anti-correlation between the *b*-value and geodetic locking before and after applying the matched filter technique. Therefore, we still need to investigate to specifically find out what the major reasons are.

REFERENCES

Aki, K. (1965), Maximum likelihood estimate of b in the formula log10 N = a - b M and its confidence limits, Bull. Earthquake Res. Inst. Univ. Tokyo, 43, 237–239.

A. Rabinovitch, et al (2001) Gutenberg-Richter-type relation for laboratory fracture-induced electromagnetic radiation, Physical review E, Volume 65,011401, DOI: 10.1103/PhysRevE.65.011401

Barckhausen, U., C. R. Ranero, R. von Huene, S. C. Cande, and H. A. Roeser, Revised tectonic boundaries in the Cocos plate off Costa Rica: Implications for the segmentation of the convergent margin and for plate tectonic models, J. Geophys. Res., 106, 19,207– 19,220, 2001.

Bayrak, Y., A. Yılmaztürk, and S. Öztürk, Lateral variation of the modal (a/b) values for the different regions of the world, J. Geodyn., 34, 653-666, 2002.

Brown, K., A. V. Newman, R. Stevens, K. McIntosh, N. Bangs, D. Chadwell, S. Bilek, G. Spinelli, S. Schwartz, L. Dorman, E. Silver, D. Hilton, M. Kastner, G. McMurty, and G. Wheat (2006), A plate boundary observatory at Costa Rica, MARGINS Newsletter, Spring 2006, 16, 19-20 (cont. 37).

Brown, J. R. et al. Deep low-frequency earthquakes in tremor localize to the plate interface in multiple subduction zones. Geophys. Res. Lett. 36, L19306 (2009).

Carena Sara (2011) subducting-plate topography and nucleation of great and giant earthquakes along the south american trench. Seismological Research Letters, Volume 82, Number 5, September/October 2011, doi: 10.1785/gssrl.82.5.629

Christeson, G. L., K. D. McIntosh, T. H. Shipley, E. R. Flueh, and H. Goedde, Structure of the Costa Rica convergent margin, offshore Nicoya Peninsula, J. Geophys. Res., 104, 25,443–25,468, 1999.

DeMets, C., A new estimate for present-day Cocos-Caribbean plate motion: Implications for slip along the Central American volcanic arc, Geophys. Res. Lett., 28, 4043–4046, 2001.

DeShon, H. R., and Schwartz, S.Y., Evidence for Serpentinization of the Forearc mantle wedge along the Nicoya Peninsula, Costa Rica, Geophys. Res. Lett., 31 (L21611), doi:10.1029/ 2004GL021179, 2004.

DeShon, H. R., S. Y. Schwartz, L. M. Dorman, A. V. Newman, V. Gonzalaz, M. Protti, T. Dixon, E. Norabuena & E. Flueh, Seismogenic zone structure along the Middle America Trench, Nicoya Peninsula, Costa Rica, from 3D local earthquake tomography using P- and S-wave data , Geoph. Jrn. Int., 164 (1), 109-124, 2006.

Dixon, T. H., GPS measurements of relative motion of the Cocos and Caribbean plates and strain accumulation across the Middle America Trench, Geophys. Res. Lett., 20, 2167– 2170, 1993.

Du chenxiao et al., in prep.

Fisher, A. T., et al., Heat flow on the incoming plate offshore Nicoya, Costa Rica margin: Implications for hydrothermal circulation and the thermal state of the subducting plate, Trans. Am. Geophys. Union (EOS), 82, F1150, 2001, [Abstract].

Ghosh, A., A. V. Newman, A.M. Thomas, G. T. Farmer, Interface locking along the subduction megathrust from microseismicity near Nicoya, Costa Rica, Geoph. Res. Lett., 35, L01301, doi:10.1029/2007GL03161, 2008.

Gutenberg, B., and C. F. Richter (1944), Frequency of earthquakes in California, Bull. Seismol. Soc. Am., 34, 185–188.

Husen, S., R. Quintero, E. Kissling, and B. Hacker, Subduction-zone structure and magmatic processes beneath Costa Rica constrained by local earthquake tomography and petrological modeling, Geophys. Journ. Int. 155 (1), 11–32. doi:10.1046/j.1365- 246X.2003.01984, 2003.

Ishimoto, M., and K. Iida (1939), Observations of earthquakes registered with the microseismograph constructed recently, Bull. Earthquake Res. Inst. Univ. Tokyo, 17, 443–478.

Joan Gomberg, et al (2010), Slow-slip phenomena in Cascadia from 2007 and beyond: A review.GSA Bulletin; July/August 2010; v. 122; no. 7/8; p. 963–978; doi: 10.1130/B30287.1; 10 Figures.

LaFemina, P., et al. (2009), Fore-arc motion and Cocos Ridge collision in Central America, Geochem. Geophys. Geosyst., 10, Q05S14, doi:10.1029/2008GC002181.

Langseth, M. G., and E. A. Silver, The Nicoya convergent margin; a region of exceptionally low heat flow, Geophys. Res. Lett., 23, 891–894, 1996.

Lundgren, P., M. Protti, A. Donnellan, M. Heflin, E. Hernandez, and D. Jefferson (1999), Seismic cycle and plate margin deformation in Costa Rica: GPS observations from 1994 to 1997, J. Geophys. Res., 104(B12), 28,915-28,926.

M. Dorman, E. Flueh, P. Lundgren, F. Pollitz, D. Sampson, Geodetic and seismic constraints on some seismogenic zone processes in Costa Rica, J. Geophys. Res., 109 (B11403), doi:10.1029/2003JB002931, 2004.

Newman, A. V., S. Y. Schwartz, V. Gonzalez, H. R. DeShon, J. M. Protti, and L. M. Dorman, Along- strike variability in the seismogenic zone below Nicoya Peninsula,

Costa Rica, Geophys. Res. Lett., 29(20), 1977, doi:10.1029/ 2002GL015409, 2002.

Norabuena, E., T. H. Dixon, S. Y. Schwartz, H. R. DeShon, A. V. Newman, M. Protti, V. Gonzalez, L.

Okada Y., Surface deformation due to shear and tensile faults in a half- space, Bull .Seismol. Soc, Am., 75,1135-1154, 1985.

Outerbridge, K. C. , T. H. Dixon, S. Y. Schwartz, J. I. Walter, M. Protti, V. Gonzalez, J. Biggers, M. Thorwart, and W. Rabbel (2010), A tremor and slip event on the Cocos-Caribbean subduction zone as measured by a global positioning system (GPS) and seismic network on the Nicoya Peninsula, Costa Rica, J. Geophys, Res., 115 B10408, doi: 10.1029/2009JB006845.

Pacheco, J. F., and L. R. Sykes, Seismic moment catalog of large, shallow earthquakes, 1900 – 1989, Bull. Seismol. Soc. Am., 82, 1306 – 1349, 1992.

Peng Zhigang and gomberg Joan (2010), An integrated perspective of the continuum between earthquakes and slow-slip phenomena. Nature Geoscience,| doi: 10.1038/ngeo940

Protti, M., F. Gundel, and K. McNally, Correlation between the age of the subducting Cocos plate and the geometry of the Wadati-Benioff zone under Nicaragua and Costa Rica, in Geologic and Tectonic Development of the Caribbean Plate Boundary in Southern Central America, edited by P. Mann, Spec. Pap. Geol. Soc. Am., 295, 309– 326, 1995a.

Protti, M., et al., The March 25, 1990 (Mw = 7.0, ML = 6.8), earthquake at the entrance of the Nicoya Gulf, Costa Rica: Its prior activity, foreshocks, aftershocks, and triggered seismicity, J. Geophys. Res., 100, 20,345– 20,358, 1995b.

Sallarès, V., J. J. Dañobeitia and, E. R. Flueh, and G. Leandro, Seismic velocity structure across the middle American landbridge in northern Costa Rica, J. Geodyn., 27, 327–344, 1999.

Sallarès, V., J. J. Dañobeitia and, and E. R. Flueh, Lithospheric structure of the Costa Rican Isthmus: Effects of subduction zone magmatism on an oceanic plateau, J.Geophys. Res., 106, 621 – 643, 2001.

Scheaffer, R. L., and J. T. McClave (1986), Probability and Statistics for Engineeres, Duxbury Press, Boston.

Scholz, C. H. (1968), The frequency-magnitude relation of microfracturing in rock and its relation to earthquakes, Bull. Seismol. Soc. Am., 58, 399 – 415.

Schorlemmer, D., S. Wiemer, and M. Wyss (2005), Variation in earthquake- size

distribution across different stress regimes, Nature, 437, 539–542, doi:10.1038/nature04094.

Sobiesiak, M., U. Meyer, S. Schmidt, H.-J. Götze, and C. M. Krawczyk, Asperity generating upper crustal sources revealed by b value and isostatic residual anomaly grids in the area of Antofagasta, Chile, J. Geophys. Res., 112, B12308, doi:10.1029/2006JB004796, 2007.

Shelly, D. R., Beroza, G. C. & Ide, S. Low-frequency earthquakes in Shikoku, Japan, and their relationship to episodic tremor and slip. Nature 442, 188–191 (2006).

Spinelli, G., D. Saffer, and M. Underwood, Hydrogeologic responses to three-dimensional temperature variability, Costa Rica subduction margin, J. Geophys. Res., 111, doi:10.1029/2004JB003436, 2006.

Stein, S., and M. Wysession (2003), An Introduction to Seismology, Earthquakes, and Earth Structure, Blackwell, Oxford, U. K.

Thomas, A. M., A. V. Newman, A. Ghosh and G. T. Farmer, Statistical Modeling of the Middle America Subduction Zone Using Interplate Seismicity, Seismo. Res. Let. , Ann. Meet. Suppl., [abstract] 2007.

Thurber, C. H., Earthquake locations and three-dimensional crustal structure in the Coyote Lake area, central California, J. Geophys. Res., 88, 8226−8236, 1983.

Utsu, T. (1965). A method for determining the value of b in a formula log n = a - bM showing the magnitude frequency for earthquakes, Geophys. Bull. Hokkaido Univ. 13, 99–103.

Vacquier, V., J. Sclater, and C. Corry, Studies in the thermal state of the earth, the 21st paper: heat-flow, eastern pacific, Bull. Earthqu. Res. Inst., 45, 375–439, 1967.

Von Huene, R., et al., Morphotectonics of the Pacific convergent margin of Costa Rica, in Geologic and Tectonic Development of the Caribbean Plate Boundary in Southern Central America, edited by P. Mann, Spec. Pap. Geol. Soc. Am., 295, 291– 307, 1995.

Walter, J. I., S. Y. Schwartz, J. M. Protti, and V. Gonzalez(2011), Persistent tremor within the northern Costa Rica seismogenic zone, Geophys, Res. Lett., 38, L01307, doi:10.1029/2010GL045586.

Warren, N. W., and G. Latham (1970), An experiment study of thermal induced micro-fracturing and its relation to volcanic seismicity, J. Geo- phys. Res., 75, 4455–4464.

Wiemer, S., and J. P. Benoit (1996), Mapping the b-value anomaly at 100 km depth in the

Alaska and New Zealand subduction zones, Geophys. Res. Lett., 23(13), 1557-1560.

Wiemer, S., and K. Katsumata (1999), Spatial variability of seismicity parameters in aftershock zones, J. Geophys. Res., 103, 13,135–13,151.

Wiemer, S., and M. Wyss (2000), Minimum magnitude of completeness in earthquake catalogs: Examples from Alaska, the western United States, and Japan, Bull. Seismol. Soc. Am., 90, 859–869.

Wiemer, S., and S. R. McNutt (1997), Variation in the frequency-magnitude distribution with depth in two volcanic areas: Mount St. Helens, Washington, and Mt. Spurr, Alaska, Geophys. Res. Lett., 24(2), 189-192.

Wyss, M. (1973), Towards a physical understanding of the earthquake frequency distribution, Geophys. J. R. Astron. Soc., 31, 341–359.

[*] Newman Andrew, Georgia Institute of Technology,

http://geophysics.eas.gatech.edu/anewman/MAT/.